PHYSICAL REVIEW B VOLUME 48, NUMBER 10 1 SEPTEMBER 1993-II

Structure of boson quantum films

B. E. Clements
Institute Laue Langevin, 38042 Grenoble Cedex, France

J. L. Epstein and E. Krotscheck
Center for Theoretical Physics, Department of Physics, Texas A&M University, College Station, Texas 77843

M. Saarela
Department of Theoretical Physics, University of Oulu, SF-90570 Oulu, Finland

(Received 25 February 1993)

We employ a quantitative microscopic theory of nonuniform quantum liquids to explore the structure and growth of thin films of ^{4}He adsorbed to a substrate. Particular emphasis is placed on answering the question of how "two dimensional" an atomic monolayer is in a realistic physical situation. An optimized variational ansatz for the wave function employing pair and triplet correlations provides a quantitatively accurate description of the zero-temperature ground state of the many-particle system. In both the two- and three-dimensional bulk-^{4}He limits, our predicted energetics are in excellent agreement with the equation of state obtained (in two dimensions) from Monte Carlo calculations and (in three dimensions) from experiments. For an adsorbate monolayer we find a binding energy slightly below that of two-dimensional ^{4}He. When more atoms are added to the system, the quantum-liquid film grows through a sequence of at least three phase transitions separating layered homogeneous phases from nonuniform surface-coverage phases. By investigating the corresponding energetics and distribution functions we elucidate the important properties of these quantum-film structures as well as quantify the departure of the monolayer from the purely two-dimensional system.

I. INTRODUCTION

Thin films of the quantum-liquid ^{4}He adsorbed to a plane substrate provide a unique opportunity to study the structure of "nearly" two-dimensional quantum liquids and, as the thickness of such an adsorbed film increases, the transition from an "essentially two-dimensional" to an "essentially three-dimensional" system at low temperatures. Microscopic many-body theory is today, partly due to a dramatic increase in computational resources, and partly due to the development of new, powerful diagrammatic techniques, capable of describing such systems with no assumptions other than the explicit forms for the interparticle interaction and the external forces acting on the system.

The study of adsorbed quantum-liquid films has in the past few years become an area of great experimental[1–7] and theoretical[8–20] activity. Unlike in bulk helium, where the number of observables and excitation mechanisms are small, these geometrically complicated systems exhibit a multitude of features which make it difficult to discern the relevant physics. A theoretical analysis of such physical systems gains therefore substantial importance.

We have previously developed microscopic approaches to study the ground-state structure and the excitation mechanisms in non-uniform quantum liquids on a semi-quantitative[8] and quantitative[21,22] level. The present paper on the zero-temperature *structure* of quantum liquid films and forthcoming papers on the low-temperature *dynamics* and *thermodynamics* of such system are devoted to an exploratory study. It is our intent to keep the description of the theoretical tools to a minimum. The reader interested in technical aspects is referred to earlier and forthcoming work.[8,21,22]

Our paper is organized as follows: In the next section we will briefly review the inhomogeneous ground-state theory. An important prerequisite for the application of any theoretical methods to thin films is that the theory has the correct limiting behavior when the film becomes two dimensional. We will show that our theory has the correct behavior by assuming a narrowly peaked density and letting the width of the distribution go to zero while keeping the particle number fixed.

Equally important to the formal consistency is the quantitative accuracy. In order to document the quality of our theoretical predictions we present, in Sec. III, results obtained in the two limiting cases, the translationally invariant two- and three-dimensional liquids. We show that the theory reproduces, in the full density regime under consideration here, the Monte Carlo data[23] for two-dimensional ^{4}He and the experimental equation of state[24] for three-dimensional ^{4}He with excellent precision. The accuracy of our predictions for the uniform phases gives us confidence that our predictions for an inhomogeneous system are of comparable accuracy. The comparison of the results of the inhomogeneous theory with the homogeneous limit *of the same theory, using identical approximations* is important to substantiate that our predictions are of physical content, and not

0163-1829/93/48(10)/7450(21)/$06.00 ©1993 The American Physical Society

possible artifacts of our approximations.

Sections IV and V are devoted to an analysis of the energetics and structure of quantum-liquid films, and to a comparison of our results with those obtained in the two-dimensional limit. A new, intriguing effect that has not been observed in our earlier, less accurate calculations is that the growth of an adsorbed film is not a continuous process but rather through a sequence of phase transitions between systems of one, two, etc., layers.[20] The actual phase diagram is complicated and depends on the substrate potential. The effect has meanwhile been observed experimentally in solid helium layers,[25] which are energetically quite similar to the liquid films investigated here.

Section VI summarizes our findings and gives a brief outlook to forthcoming work. The Appendix describes our treatment of triplet correlations.

II. GROUND-STATE THEORY

The microscopic description of a strongly interacting system conventionally starts with an empirical Hamiltonian

$$H=\sum_{i=1}^{N}\left\{-\frac{\hbar^2}{2m}\nabla_i^2+U_{\rm ext}(\mathbf{r}_i)\right\}+\sum_{1\le i<j\le N}v(|\mathbf{r}_i-\mathbf{r}_j|),\qquad(2.1)$$

where $U_{\rm ext}(\mathbf{r})$ is an external potential, and $v(|\mathbf{r}_i-\mathbf{r}_j|)$ is the interaction between individual particles, which we take to be the Aziz potential.[26]

The ground-state wave function for a system of N identical bosons with coordinates $\mathbf{r}_1,\ldots,\mathbf{r}_N$ is approximated by a variational ansatz[27] of the form

$$\Psi_0(\mathbf{r}_1,\ldots,\mathbf{r}_N)=\exp\frac{1}{2}\left\{\sum_i u_1(\mathbf{r}_i)+\sum_{i<j}u_2(\mathbf{r}_i,\mathbf{r}_j)+\sum_{i<j<k}u_3(\mathbf{r}_i,\mathbf{r}_j,\mathbf{r}_k)+\ldots\right\}.\qquad(2.2)$$

The one-body function $u_1(\mathbf{r})$ describes the spatial structure of the system, and the two-body function $u_2(\mathbf{r}_i,\mathbf{r}_j)$ describes the short- and long-range correlations between pairs of particles. Triplet correlations are needed to provide quantitative agreement between theoretical predictions and the experimental equation of state,[28–30] and contribute visibly to the nearest-neighbor peak of the pair distribution function. The correlation functions $u_n(\mathbf{r},\ldots,\mathbf{r_n})$ are determined by minimization of the energy-expectation value E_0:[31]

$$\frac{\delta E_0}{\delta u_n(\mathbf{r},\ldots,\mathbf{r_n})}=0.\qquad(2.3)$$

The extension of the optimized hypernetted-chain Euler-Lagrange (HNC-EL) theory to the *nonuniform* quantum liquids is based on the same *formal* ideas as theory of the homogeneous ground state.[28–30,32] To handle the symmetry breaking is not merely a *large-scale* computational problem, the theory must be formulated such that the solution of the equations is numerically tractable and more importantly, the iteration scheme is stable against numerical noise that can ultimately lead to divergent solutions. The general theory of nonuniform ^{4}He and in particular the description of the interpretation and solution of the equations has been described in several papers.[8,33] The existence of a stable iteration scheme is especially important in the present system which has a phase diagram complicated by the presence of many phase transitions. Indeed this complication along with complicated geometry will make the study of this system by stochastic methods extremely cumbersome.

The inclusion of triplet correlations and "elementary diagrams" provides quantitative agreement with experiments, but does not change the essential features of the theory. Necessary details and our working formulas for the inclusion of triplet correlations will be given in the Appendix. The method is the direct generalization of the work of Refs. 28–30 and 32 to nonuniform quantum liquids.

The HNC equations provide relationships between the one-body density $\rho_1(\mathbf{r})$, the pair and triplet distribution functions $g(\mathbf{r}_i,\mathbf{r}_j)$ and $g_3(\mathbf{r}_i,\mathbf{r}_j,\mathbf{r}_k)$, and the correlation functions $u_n(\mathbf{r}_1,\ldots,\mathbf{r}_n)$. These relationships are used to rewrite the ground-state energy in terms of the physically observable quantities $\rho_1(\mathbf{r})$ and $g(\mathbf{r},\mathbf{r}')$ (cf. the Appendix):

$$E_0=E_0[\rho_1(\mathbf{r}),g(\mathbf{r},\mathbf{r}')]=T+V_{\rm ext}+E_c.\qquad(2.4)$$

Here, T is the kinetic energy of a noninteracting model system whose ground-state wave function is $\sqrt{\rho_1(\mathbf{r})}$,

$$T=\frac{\hbar^2}{2m}\int d^3r\left|\nabla\sqrt{\rho_1(\mathbf{r})}\right|^2.\qquad(2.5)$$

$V_{\rm ext}$ is the energy of the particles in the external potential

$$V_{\rm ext}=\int d^3r\,U_{\rm ext}(\mathbf{r})\rho_1(\mathbf{r}).\qquad(2.6)$$

The "correlation" energy, E_c, is written as the sum of two parts,

$$E_c=\Delta E^{(2)}+\Delta E^{(3)},\qquad(2.7)$$

where $\Delta E^{(2)}$ can be expressed entirely in terms of pair distribution functions,

$$\Delta E^{(2)}=\Delta E^{(2)}[\rho_1(\mathbf{r}),g(\mathbf{r},\mathbf{r}')],\qquad(2.8)$$

and $\Delta E^{(3)}$ also contains triplet correlations. Explicit formulas are given in Eqs. (A16) and (A27) in the Appendix.

The representation of the variational ground-state energy given there, and the HNC relations (A14) and (A15) are the basis of the HNC-EL theory. Note that the correlation energy is expressed entirely in terms of physical observables and quantities derived from them.

Since, as shown in the Appendix, the triplet correlations can, within an adequate approximation, be expressed explicitly as a functional of the pair distribution function and the one-body density, we can think of the HNC energy as a functional of $\rho_1(\mathbf{r})$ and $g_2(\mathbf{r}_1,\mathbf{r}_2)$. Given this energy functional, the ground-state structure of the adsorbed film is now calculated by minimization of the ground-state energy with respect to the one-body density and the pair distribution function for fixed particle number per unit area. The resulting one-body equation

$$\left[-\frac{\hbar^2}{2m}\nabla^2 + U_{\rm ext}(\mathbf{r}) + V_H(\mathbf{r})\right]\sqrt{\rho_1(\mathbf{r})} = \mu\sqrt{\rho_1(\mathbf{r})} \quad (2.9)$$

has the formal structure of a Hartree equation, where

$$V_H(\mathbf{r}) = \frac{\delta E_c}{\delta \rho_1(\mathbf{r})} \quad (2.10)$$

is a self-consistent one-body potential. Of course, its analytic structure is more complicated than the ordinary Hartree potential appearing in theories of weakly interacting systems. Rather, one may think of the HNC-EL theory as of a version of density-functional theory with a highly nonlocal correlation-energy functional. An essential point, which is not present in conventional implementations of density-functional theory such as the local-density approximation, gradient corrections, or nonlocal functionals employing an effective interaction, is that the HNC-EL density functional *exists only for physically realizable densities.*

We consider here a plane surface geometry in which a substrate is located at $z < 0$, and assume translational invariance in the x-y plane. In this geometry, the one-body density $\rho_1(\mathbf{r})$ depends only on the distance z from the substrate. Two-body quantities like the pair distribution function $g(\mathbf{r},\mathbf{r}')$ depend on the distance of each of the particles from the substrate, and the distance between the two particles parallel to the surface. Resulting quantities of the calculation are the ground-state energy per particle E/N, the chemical potential μ, the one-body density $\rho_1(\mathbf{r})$, and the pair distribution function $g(\mathbf{r},\mathbf{r}')$ as a function of the surface coverage

$$n = \int_{-\infty}^{\infty} dz \rho_1(z). \quad (2.11)$$

For the purpose of the present physical situation it is important to verify that the energy functional behaves correctly in the limit that the system becomes rigorously two dimensional. To take the limit, we imagine the following process: We place the system in an external potential $U_{\rm ext}(z)$ as above. Keeping the particle number (2.11) per unit area fixed, we change the external potential such that the density becomes more and more localized in the z direction. In that limit, the *correlation energy* E_c [Eq. (2.7)] should go towards the correlation energy *of the corresponding two-dimensional system.*

To see that the HNC theory behaves correctly in the two-dimensional limit described above, we start from the representation (A16). We restrict ourselves for this exercise to pair correlations, the inclusion of triplet correlations leads to no further insight. First, the terms E_R and E_Q are rewritten as

$$E_R = \frac{1}{2!}\int d^3r_1 d^3r_2 \rho_1(\mathbf{r}_1)\rho_1(\mathbf{r}_2)\left\{ g(\mathbf{r}_1,\mathbf{r}_2)v(|\mathbf{r}_1-\mathbf{r}_2|) + \frac{\hbar^2}{2m}\left|\nabla_1\sqrt{g(\mathbf{r}_1,\mathbf{r}_2)}\right|^2 - \frac{\hbar^2}{8m}\left[\nabla_1 g(\mathbf{r}_1,\mathbf{r}_2)\cdot\nabla_1 E(\mathbf{r}_1,\mathbf{r}_2) + \text{same for } 1 \leftrightarrow 2\right]\right\} \quad (2.12)$$

and

$$E_Q = -\frac{\hbar^2}{16m}\int d^3r_1 d^3r_2 \rho_1(\mathbf{r}_1)\rho_1(\mathbf{r}_2)\left[\nabla_1 g(\mathbf{r}_1,\mathbf{r}_2)\cdot\nabla_1 N(\mathbf{r}_1,\mathbf{r}_2) + \text{same for } 1 \leftrightarrow 2\right], \quad (2.13)$$

where $N(\mathbf{r}_1,\mathbf{r}_2)$ is the sum of "nodal diagrams" given by the integral equation (A15).

The purpose of the integrations by parts was to remove all density derivatives. After this is accomplished, we can take the limit of a two-dimensional (2D) system: Let

$$\rho^{\rm 2D}(\mathbf{r}) = n\delta(z). \quad (2.14)$$

This leads to (leaving out the elementary diagrams for brevity)

$$E_R^{\rm 2D} = \frac{An^2}{2}\int d^2r_\parallel \left[g(0,0,r_\parallel)v(r_\parallel) + \frac{\hbar^2}{m}|\nabla_\parallel\sqrt{g(0,0,r_\parallel)}|^2\right] + \frac{A\hbar^2 n^2}{2m}\int d^2r_\parallel \left|\frac{d}{dz}\sqrt{g(z,0,r_\parallel)}_{z=0}\right|^2, \quad (2.15)$$

where A is the normalization area. The first term in Eq. (2.15) is the E_R for a two-dimensional uniform system. The second term vanishes since, due to symmetry, $g(z,0,r_{\|}) = g(-z,0,r_{\|})$. The consideration excludes situations where $g(z,0,r_{\|})$ has a cusp at $z=0$, however, this happens only for the electron gas and only for $r_{\|}=0$, in other words in a volume of mesh zero.

An analogous argument can be carried out for the elementary diagrams and for the second term, E_Q [Eq. (2.13)] and the elementary diagram contributions. The existence of the proper two-dimensional limit appears, superficially, to be an academic exercise. The unsurprising result simply reflects an obvious consistency for the theory which should be made before any attempt to understand the transition from the monolayer to a three-dimensional system. We therefore hasten to point out that one of the most popular approaches to nonuniform quantum systems, namely the local-density approximation to density-functional theory, *diverges* in the two-dimensional limit for all but a linear energy functional.

In preparation for the physical arguments of the next section, and also for the definitions used in the Appendix, we briefly discuss the two-body equation

$$\frac{\delta E_c}{\delta g(\mathbf{r},\mathbf{r}')} = 0. \tag{2.16}$$

Determining the pair correlations by optimization [as opposed to an "intelligent guess" for the pair correlation function $u_2(\mathbf{r},\mathbf{r}')$] has a number of significant advantages: First, the optimized theory is formulated entirely in terms of physical observables, e.g., the one- and two-body densities. In fact, the Euler equation can be derived, from an approximate summation of Feynman diagrams, without ever introducing the correlation functions. Second, the optimization eliminates any prejudice on the structure of the system we might have. Third, the additional computational demands introduced from the optimization is insignificant relative to solving the HNC equations for a single trial function $u_2(\mathbf{r},\mathbf{r}')$. Besides the practical advantage of providing the best possible wave function in the given function space, one can show generally that *the Euler equations do not give (unphysical) solutions if the assumed geometry of the system under consideration is unstable against infinitesimal density fluctuations.* For example, Euler equations will cease to have solutions if one makes the incorrect assumption that the liquid will be in a uniform state, and then attempt to lower the density below the thermodynamic *spinodal line* where the incompressibility becomes negative.[34] The Euler equations will have solutions only if they are defined in a general enough space that includes the broken-symmetry phase; in this example, the liquid-droplet–gas coexistence. Consequently, one has confidence that the theory describes the correct physics, in particular, in the vicinity of a liquid-gas phase transition. Our numerical examples to be studied below are a beautiful demonstration of the physical content and the practical power of optimized HNC theory.

The two-body Euler equation is best formulated in terms of the (real-space) static structure function

$$S(\mathbf{r},\mathbf{r}') = \delta(\mathbf{r}-\mathbf{r}') + \sqrt{\rho_1(\mathbf{r})\rho_1(\mathbf{r}')}[g(\mathbf{r},\mathbf{r}')-1], \tag{2.17}$$

a one-body Hamiltonian

$$H_1 = -\frac{\hbar^2}{2m}\frac{1}{\sqrt{\rho_1(\mathbf{r})}}\nabla\rho_1(\mathbf{r})\nabla\frac{1}{\sqrt{\rho_1(\mathbf{r})}}, \tag{2.18}$$

and the so-called *particle-hole interaction* $V_{\text{p-h}}(\mathbf{r}_1,\mathbf{r}_2)$. In terms of these quantities, the two-body Euler equation can be written in the form

$$\left[S^{-1} * H_1 * S^{-1}\right](\mathbf{r}_1,\mathbf{r}_2) = \delta(\mathbf{r}_1-\mathbf{r}_2)H_1(\mathbf{r}_1) + 2\tilde{V}_{\text{p-h}}(\mathbf{r}_1,\mathbf{r}_2). \tag{2.19}$$

Above we have introduced the convolution product between two functions

$$[A * B](\mathbf{r}_1,\mathbf{r}_2) \equiv \int d^3r_3 A(\mathbf{r}_1,\mathbf{r}_3)B(\mathbf{r}_3,\mathbf{r}_2) \tag{2.20}$$

and the "tilde" notation

$$\tilde{V}_{\text{p-h}}(\mathbf{r}_1,\mathbf{r}_2) \equiv \sqrt{\rho_1(\mathbf{r}_1)}V_{\text{p-h}}(\mathbf{r}_1,\mathbf{r}_2)\sqrt{\rho_1(\mathbf{r}_2)}. \tag{2.21}$$

One-body quantities such as $H_1(\mathbf{r})$ are diagonal in this representation, and the inverse of the static structure function is to be understood in the sense of the convolution product (2.20). The particle-hole interaction can be represented in terms of the one-body density and the diagrammatic quantities defined in the Appendix, its analytic form is irrelevant here. An important alternative definition of $V_{\text{p-h}}(\mathbf{r},\mathbf{r}')$ is

$$V_{\text{p-h}}(\mathbf{r},\mathbf{r}') \equiv \frac{\delta^2 E_c}{\delta\rho_1(\mathbf{r})\delta\rho_1(\mathbf{r}')}, \tag{2.22}$$

but the definitions of $V_{\text{p-h}}(\mathbf{r},\mathbf{r}')$ and (2.22) are analytically identical only if *all* elementary diagrams are included.

The numerical solution of the two-body Euler equation (2.19) is intimately connected to the Feynman theory of collective excitations. We solve the eigenvalue problem

$$[H_1 + 2\tilde{V}_{\text{p-h}}] * H_1\psi^{(l)} = \hbar^2\omega_l^2\psi^{(l)}. \tag{2.23}$$

The eigenstates $\psi^{(l)}$ of Eq. (2.23) are orthogonal in the metric defined by the one-body operator H_1; the most convenient normalization is

$$(\psi^{(l)}|H_1|\psi^{(l')}) = \hbar\omega_l\delta_{l,l'}. \tag{2.24}$$

The eigenstates of the adjoint equation

$$H_1 * [H_1 + 2\tilde{V}_{\text{p-h}}]\phi^{(l)} = \hbar^2\omega_l^2\phi^{(l)} \tag{2.25}$$

are

$$\phi^{(l)} = \frac{1}{\hbar\omega_l}H_1\psi^{(l)}. \tag{2.26}$$

The static structure function is obtained from the eigenstates by a normal-mode expansion

$$S(\mathbf{r}_1,\mathbf{r}_2) = \sum_l \phi^{(l)}(\mathbf{r}_1)\phi^{(l)}(\mathbf{r}_2). \tag{2.27}$$

While the normal-mode decomposition gives, for the purpose of this paper, just a convenient vehicle to solve the nonlinear equation (2.19), we note that the eigenfunctions of the problem (2.23) are closely related to the excitation functions in the Feynman theory of collective excitations. The eigenfunctions of the adjoint equation are the transition densities in that theory.[35] Correspondingly, the energies $\hbar\omega_\ell$ are the excitation energies in the Feynman theory. From Eq. (2.19), it is evident that the operator $\delta(\mathbf{r}_1 - \mathbf{r}_2)H_1(\mathbf{r}_1) + 2\tilde{V}_{\text{p-h}}(\mathbf{r}_1,\mathbf{r}_2)$ must be positive definite to have a solution. If this is so, the long-wavelength limit of the lowest-lying excitation is, in the plane surface geometry, given by

$$\omega(k_\parallel) = c_3 k_\parallel \qquad (k_\parallel \to 0+), \tag{2.28}$$

where c_3 is the third-sound velocity, and $k_\parallel$ the momentum parallel to the surface. This velocity can be calculated from the long-wavelength limit of the particle-hole interaction.[35] In the geometry used here, the particle-hole interaction is a function of the distance (z,z') of both particles from the substrate, and their relative distance $r_\parallel$ parallel to the surface. Fourier transforming the parallel coordinate yields a mixed representation $\tilde{V}_{\text{p}-\text{h}}(z,z',k_\parallel)$ for the particle-hole interaction, and a similar representation for

$$H_1(z,k_\parallel) = -\frac{\hbar^2}{2m}\frac{1}{\sqrt{\rho_1(z)}}\frac{d}{dz}\rho_1(z)\frac{d}{dz}\frac{1}{\sqrt{\rho_1(z)}} + \frac{\hbar^2 k_\parallel^2}{2m}. \tag{2.29}$$

In terms of these mixed quantities, the long-wavelength limit (2.28) is

$$m\bar{c}_3^2 = \frac{1}{2}\frac{n}{\left(\sqrt{\rho_1}\middle|[H_1(0+) + 2\tilde{V}_{\text{p-h}}(0+)]^{-1}\middle|\sqrt{\rho_1}\right)}, \tag{2.30}$$

where $H_1(0+)$ and $\tilde{V}_{\text{p-h}}(0+)$ are the operators $H_1(z,k_\parallel)$ and $\tilde{V}_{\text{p-h}}(z,z',k_\parallel)$ in the limit $k_\parallel \to 0+$.

An alternative definition of the third-sound velocity can be obtained from the hydrodynamic relationship[35–38]

$$mc_3^2 = n\frac{d\mu}{dn}. \tag{2.31}$$

When comparing the long-wavelength limit of the collective excitations (2.28) and the hydrodynamic definition (2.31), the same precautions apply as in the discussion of the equivalence of the particle-hole interaction originating from the optimization and from (2.22): They are identical only in an exact theory.[35]

We conclude this section by a word of caution about the identification of the long-wavelength excitations with "third sound." With third sound one normally means a surface excitation that is driven by the substrate potential. However, in strongly confined situations, such an excitation may have a very high energy, and the lowest-lying mode may indeed be a "two-dimensional" phonon. A clean identification of the physical nature of a specific excitation can be made only by examining the transition density and the particle currents. We defer further elaboration on this important point until a forthcoming work. At this point, it is, however, worth noting that Eq. (2.31) does *not* imply that one is dealing with surface excitations. In a *homogeneous* system, where a pressure can be defined, Eq. (2.31) reduces to the hydrodynamic relationship

$$mc^2 = \frac{dP}{dn}, \tag{2.32}$$

however, Eq. (2.31) is more general since it is true no matter whether the lowest-lying excitation is a surface or a volume mode.

III. HOMOGENEOUS ^{4}He IN TWO AND THREE DIMENSIONS

The ground state of the three-dimensional (3D), homogeneous ^{4}He is a well-studied system both theoretically and experimentally. In the case of homogeneous, two-dimensional (2D) ^{4}He there are no experimental results available for comparison and we must rely on the Monte Carlo data.[23] The purpose of presenting our results from the variational approach for these two systems is twofold: We want to confirm that our method gives a good description of these limiting cases before analyzing the *inhomogeneous* system. We also show some results which are not easily accessible with the Monte Carlo method (e.g., the speed of sound and the particle-hole interaction) but are nevertheless of basic and experimental interest.

We present results for the entire density range of the liquid phase. The experimentally accessible lower limit of the density for the 3D system is the saturation density of 0.0218 Å^{-3}, but theoretically one can lower the density and study the system with a negative pressure down to the spinodal point where the system becomes unstable against density fluctuations. The freezing density of the 3D liquid at zero temperature and 25 atm pressure is about 0.026 Å^{-3}. Theoretically we find the liquid solution past that density, but a precursor of the solidification can be seen in the excitation spectrum[39,40] of the multipole components of the density fluctuations. As expected, the energy of the ℓ=6 multipole state becomes negative in the long-wavelength limit before the Euler equation ceases to have a homogeneous solution. The solution of the Euler equation disappears at the point where the system becomes *locally* unstable whereas the thermodynamic path to solidification (approached from the liquid side) proceeds on a curve of metastability. The situation is the well-known supercooling of a liquid which requires a small perturbation to solidify. In the case of 2D system the liquid solution is found for the density range from 0.031 Å^{-2} to 0.07 Å^{-2}. The lower limit is determined by the spinodal point, and in the upper limit the pair distribution function has long-range oscillations reflecting the long-range order of the solid phase. Here the peak of the structure function approaches the limiting value of two. It is interesting to note that the liquid densities of the 3D and 2D systems barely overlap. The interparticle spacing of the 2D upper limit 0.07 Å^{-2} corresponds to the 3D density of 0.0185 Å^{-3}. We are therefore testing our method from the interparticle distance of 3.3 Å up to 5.8 Å.

In the previous section the expression for the correlation energy per particle (2.7) was divided into two parts. The HNC approximation part contains the contribution from the pair distribution functions, including all elementary diagrams that can be expressed in terms of $g(\mathbf{r},\mathbf{r}')$. We calculate explicitly the four-body elementary diagram and a set of five-body diagrams specified in the Appendix. The contribution of the higher-order diagrams is estimated by multiplying the four- and five-body diagrams by a factor of 1.4. This enhancement factor is determined by fitting the experimental energy of *three-dimensional* liquid ^{4}He at experimental saturation density. The second part contains all the triplet correlations. The expressions for both of these contributions are given in the Appendix. The results for the energy per particle as a function of density are shown in Fig. 1. The agreement with the experiments and the Monte Carlo results is quite satisfactory within the entire density range. In Fig. 1 we have also included a cubic polynomial fit of the form

$$\frac{E}{N}=\frac{E_0}{N}+B\left(\frac{\rho-\rho_0}{\rho_0}\right)^2+C\left(\frac{\rho-\rho_0}{\rho_0}\right)^3 \qquad (3.1)$$

to the experiments for the 3D system and Monte Carlo results for the 2D system. The parameters are listed in Table I. Of course, this polynomial is valid only within the density range where the fitting is done. Reliable continuation to smaller densities would require independent information on the derivatives of the energy with respect to density, i.e., on the pressure and incompressibility. That is available for the 3D case,[41] but not for the 2D case. As a consequence there is some uncertainty in determination of the density where the 2D speed of sound becomes zero.

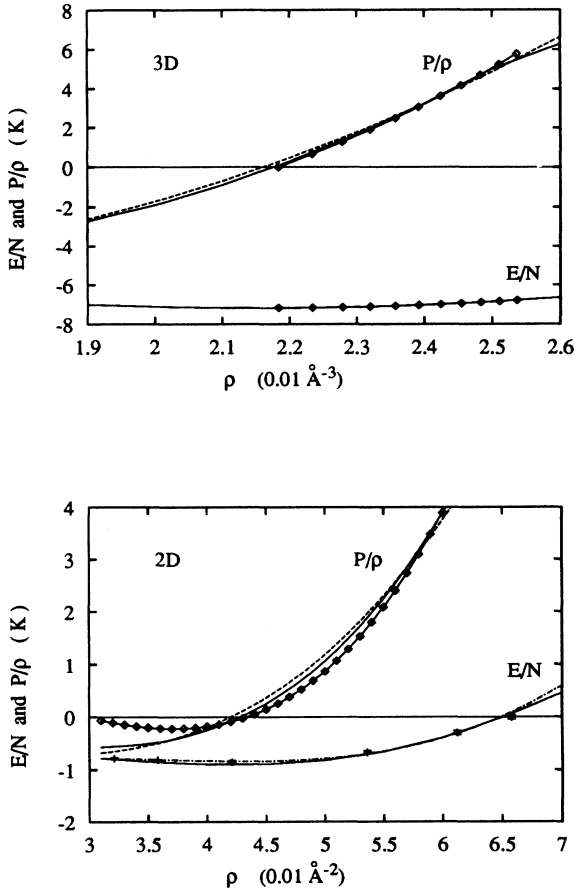

FIG. 1. The energy/particle and pressure/density as a function of density for 3D and 2D liquid ^{4}He. In the 3D case the comparison is done with experiments (Ref. 52) (lines with diamonds), and in the 2D case with the Monte Carlo results (Ref. 23) (dots with error bars). The dash-dotted line is the cubic polynomial fit to the Monte Carlo results and the pressure (line with diamonds) is calculated from that fit. The solid lines show the calculated E/N and P/ρ and the dashed lines for the pressure are taken from the cubic polynomial fit to the energy per particle.

In Fig. 1 we also present the pressure per density as a function of density. In the 3D system we compare with experiments whereas in the 2D case we calculate the pressure by differentiating the cubic polynomial fit of Eq. (3.1) to the Monte Carlo data,

$$\frac{P}{\rho}=\rho\frac{d(E/N)}{d\rho}. \qquad (3.2)$$

The saturation densities, ρ=0.0218 Å^{-3} for 3D and ρ=0.0436 Å^{-2} for the 2D fluid, are well reproduced by the theory as shown in Table I. At the negative pressure the variational and Monte Carlo results differ notably; we assign this to the uncertainties in the fitting pointed out above. An important check of consistency of our results shown in Fig. 1 is to calculate the pressure by differentiating the cubic polynomial fit to the calculated energy per particle. An accurate theory will yield values that agree with the pressure obtained variationally.

The incompressibility of the homogeneous system, $mc^2 = dP/d\rho$, defined similar to Eq. (2.31), is evaluated from the polynomial fits and shown in Fig. 2. The spinodal point determined from the experimental results for 3D system is ρ=0.016 Å^{-3} compared with our result ρ=0.015 Å^{-3} and from the 2D Monte Carlo results ρ=0.037 Å^{-2} compared with our result ρ=0.031 Å^{-2}. As pointed out earlier these results are very sensitive to the

TABLE I. The parameters fitted to the equation of state using the cubic polynomial of Eq. (3.1). The fitting is done to our theoretical results, to experiments in the 3D system and to the 2D Monte Carlo results.

	3D		2D	
Parameter	Experimental	Theory	Monte Carlo	Theory
E_0/N	-7.17	-7.185	-0.8357	-0.9057
ρ_0	0.02182	0.02162	0.04356	0.0420
B	13.45	12.78	1.659	2.254
C	7.80	2.73	3.493	1.259

parametrization of the fitting polynomial because they are calculated from the second derivative. Another consistency check of the variational approach is to calculate the incompressibility from the slope of the structure function or equivalently from the particle-hole potential in the long-wavelength limit. These results agree with the hydrodynamic incompressibility only at low densities. The difference increases with increasing density. The diagrammatic origin of that problem is discussed in detail in Ref. 32.

The structure of the liquid is revealed by studying the pair distribution and structure functions. In Fig. 3 we compare the calculated and experimental results for the 3D system. The overall agreement at the saturation density is quite good and of the same quality as between different sets of experiments. Similar agreement is found in Fig. 4 between 2D variational and Monte Carlo results near the saturation density, but closer to the solidification there is a clear difference in the position of the peaks of both the structure and the pair distribution functions.

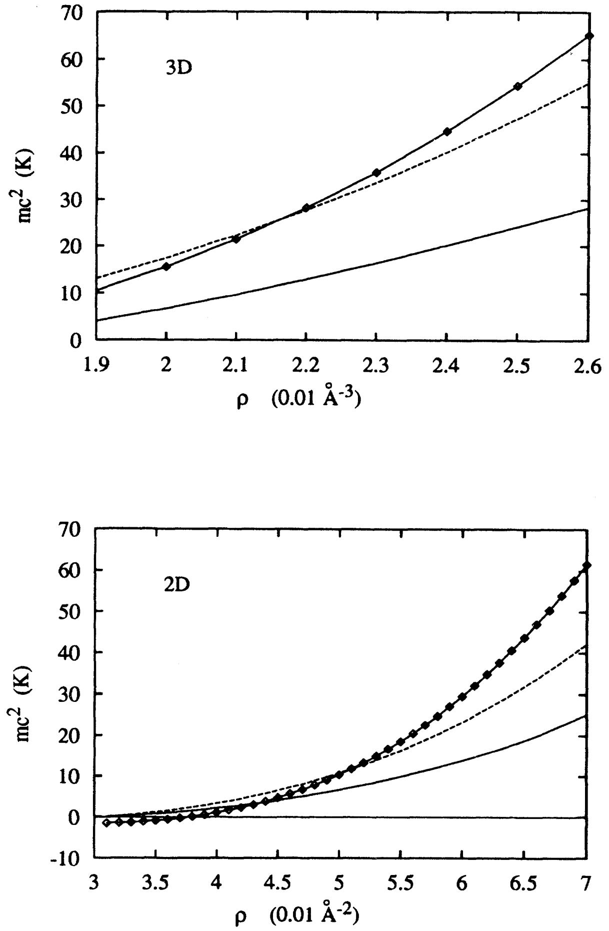

FIG. 2. The incompressibility as a function of density for 3D and 2D liquid ^{4}He. In the 3D case the comparison is done with the incompressibility calculated from the cubic polynomial fit to the experimental equation of state (Ref. 52) and in the 2D case the fit is done to the Monte Carlo results (Ref. 23) (lines with diamonds). The solid lines are the calculated incompressibilities taken from the particle-hole potential and the dashed lines are from the cubic polynomial fit to the equation of state.

In Fig. 5 we show the structure functions for the whole density range in two and three dimensions. In the 2D case we demonstrate that at the low-density limit the slope of $S(k)$ at $k = 0$ becomes infinite as the speed of sound approaches zero. In the high-density limit the first peaks of the structure function increase strongly approaching the critical value of max$[S(k)]$=2. There the iteration convergence of the Euler equation becomes very slow signaling an instability to solidification. The same signal is seen from the pair distribution function in Fig. 6. The oscillations in $g(r)$ become longer and longer range with increasing density ultimately extending throughout the whole sample (which in our calculations is 36 Å).

Finally we show the results for the particle-hole potentials in Figs. 7 and 8. The value of $V_{\text{p-h}}(k)$ at $k = 0$ determines the incompressibility and is used in Fig. 2. These quantities are called pseudopotentials in the semiphenomenological theory by Aldrich and Pines.[42] These authors used theoretical considerations such as the short-range repulsion and exact sum rules along with experimental information (e.g., the speed of sound) in determining their pseudopotentials. In momentum space, our potentials are very similar to the pseudopotentials, but

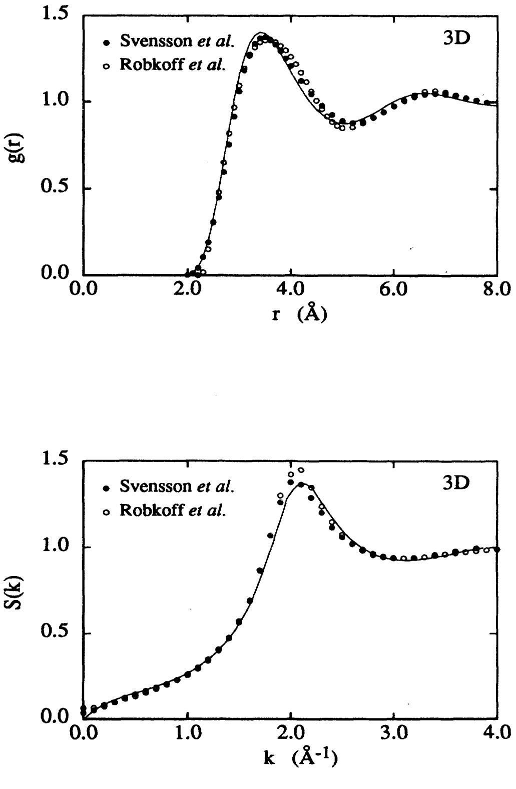

FIG. 3. The calculated pair distribution functions $g(r)$ and structure functions $S(k)$ for 3D *bulk* ^{4}He (solid lines) at a density $\rho = 0.022\,\text{Å}^{-3}$ compared with experiments by Svensson *et al.* (Ref. 46) (dots) and Robkoff *et al.* (Ref. 47) (circles). The theoretical results are from Ref. 32.

we find more structure in coordinate space. The qualitative features of the effective potentials are easily traced back to different physical effects: First, the effective interaction will not have a hard core due to short-ranged screening which is microscopically described by the summing of all ladder diagrams. Second, due to the kinetic energy induced by the core exclusion, the repulsive cores of the atoms will appear to be slightly larger than the core of an isolated helium atom. The microscopic theory predicts that these effects produce somewhat more structure than estimated by Aldrich and Pines.[42] Third, due to the presence of other particles, the attractive part is enhanced. To document these effects, we show in Fig. 7 the particle-hole interaction in bulk ^{4}He as a function of density and compare this effective interaction with the bare Aziz potential. Both effects outlined above are clearly seen. The peak near the zero of the Aziz potential is missing in the Aldrich and Pines pseudopotentials. We also find that the attraction of the Aziz potential is shifted in $V_{\rm p-h}(r)$ which is not the case in the pseudopotentials.

IV. QUANTUM-FILM ENERGETICS

With these remarks made, we may proceed to study the energetics of adsorbed thin films. It is useful to begin by discussing what one should expect for the growth scenario of these films. We start with a plane substrate which contains no helium or an inert number of layers of solid helium. As the helium atoms are adsorbed to a substrate of either host atoms or a solid layer of helium atoms, one would expect that first a liquid atomic monolayer is formed. We will refer to this layer as to the "first" layer of atoms, independently of whether the substrate itself consists of solid layers of ^{4}He. At very low densities, this first liquid layer will form a low-density "almost" two-dimensional liquid; its energetics and equilibrium properties should be reasonably well described by those of a rigorously two-dimensional system. However, such a "two-dimensional liquid" cannot be formed at all densities: The saturation density of a two-dimensional liquid of ^{4}He, $\rho_{\rm 2D}$, is known[23] to be approximately 0.043 Å^{-2}. But below a certain minimum

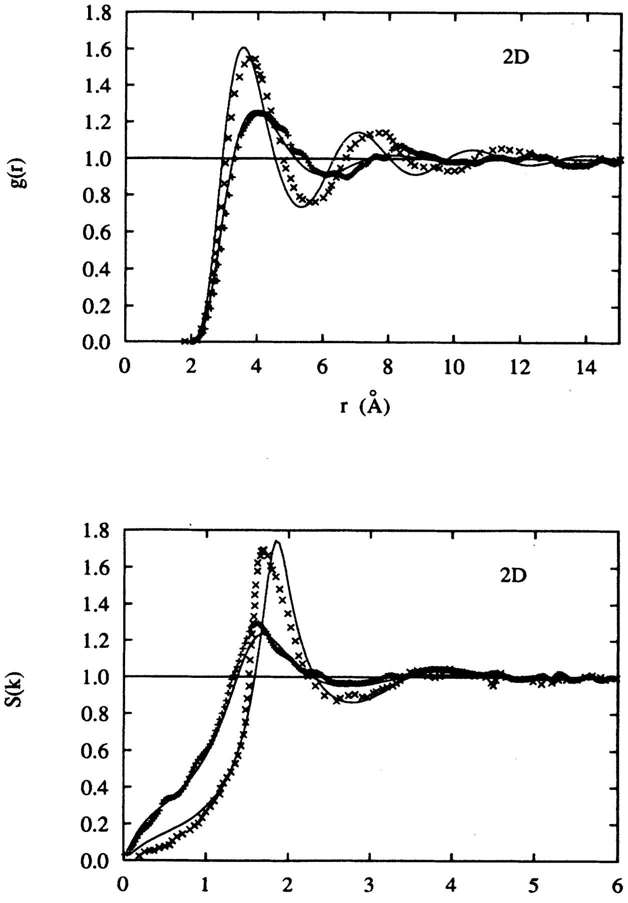

FIG. 4. The pair distribution functions and structure functions for 2D *bulk* ^{4}He (solid lines) compared with the Monte Carlo results (Ref. 23). We show two densities, $\rho = 0.0421$ Å^{-2} which is near equilibrium (+ symbols) and $\rho = 0.0658$ Å^{-2} ($\times$ symbols) which is a density just before freezing. The curves with higher peaks correspond to higher density.

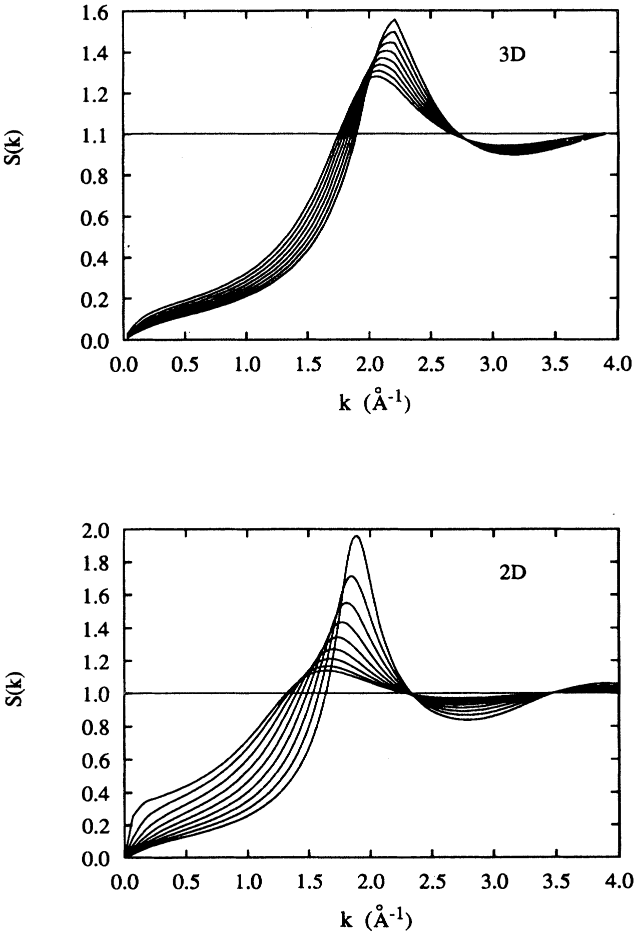

FIG. 5. The structure functions for *bulk* ^{4}He. In the 3D case they are shown for the densities $\rho = 0.019, 0.020, \ldots, 0.026$ Å^{-3} and in the 2D case for $\rho = 0.031, 0.035, 0.040, \ldots, 0.07$ Å^{-2}. The function with the highest peak corresponds to the highest density.

density the *two-dimensional* incompressibility vanishes and the system moves into a state of spinodal decomposition, i.e., two-dimensional ^{4}He "clusters" coexisting with the vacuum. An estimate derived from the analytic fit of the Monte Carlo results given in Ref. 23 for $\rho_{2\mathrm{D}_{\min}}$ is 0.037 Å^{-2}, but this value depends somewhat on the fitting functions. It is important to note that the saturation density $\rho_{2\mathrm{D}}$ is considerably below the saturation density, $\rho_{3\mathrm{D}}$, of three-dimensional ^{4}He, which would translate into a surface density of $\rho_{3\mathrm{D}}^{2/3} \approx 0.077$ Å^{-2}. Therefore, by adding further atoms to the liquid, the two-dimensional system must become highly compressed in order to approach the bulk equilibrium density. A density will eventually be reached at which it becomes energetically favorable to elevate particles to a next layer before the previous layer can be further compressed. In this situation "patches" of ^{4}He can form on the previous layer, and the translational symmetry parallel to the helium surface is spontaneously broken. Formally, the effect is described by the fact that the chemical potential is no longer a monotonic function of the surface coverage, or equivalently, that the third-sound velocity (2.31), becomes imaginary. The qualitative physical scenario described above will lead to a sequence of "islands" of stability of the physical system where the incompressibility is positive, leaving certain unstable coverages out. It is obvious that the feature of the Euler equations that they do not have solutions for an unstable geometry is particularly relevant in the scenario we have described above.

The above arguments are of course qualitative and *assume* that a liquid monolayer can reasonably well be approximated by a two-dimensional liquid. To what extent this is true can only be determined by allowing the liquid to have a finite extension in the direction of the third dimension. To accommodate such a situation, we must study, similar to the limiting process that we have carried out in the previous section, the three-dimensional system in an external potential. To study an experimentally relevant situation, we examine several model potentials for liquid helium adsorbed on a solid substrate. The first one represents two layers of solid helium on graphite. The two planes of solid helium are modeled by averaging Lennard-Jones potentials over a plane,

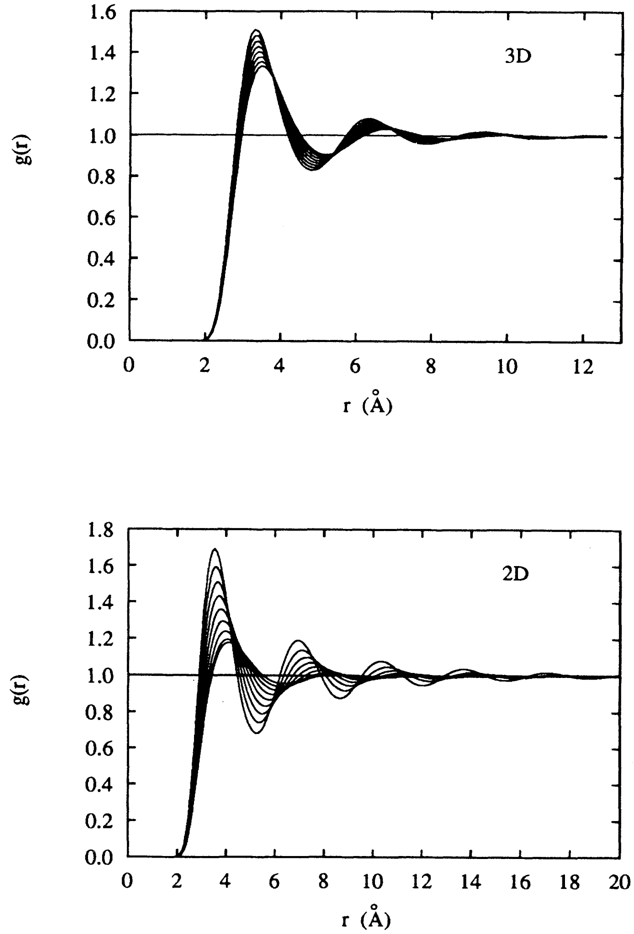

FIG. 6. The pair distribution functions for *bulk* ^{4}He. The range of densities is the same as in Fig. 5. The function with the highest peak corresponds to the highest density.

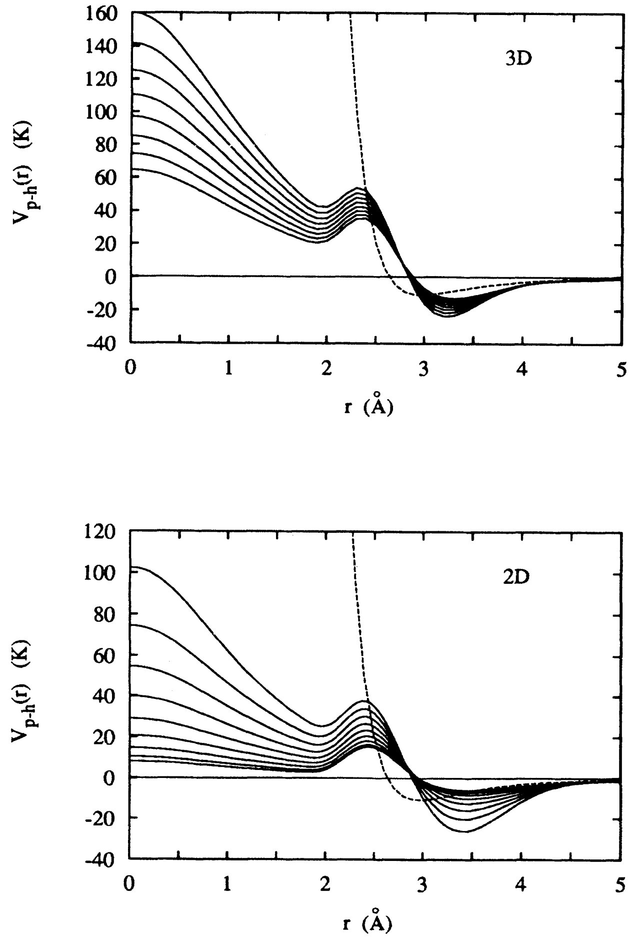

FIG. 7. The particle-hole potentials are shown for 3D and 2D *bulk* ^{4}He. The densities are the same as in Fig. 5. The potential with the most attractive well and the most repulsive core corresponds to the highest density (solid lines). Also shown is the bare Aziz potential (dashed line).

$$U_i(z) = 4\pi\epsilon n_i\sigma^2\left[\frac{1}{5}\left(\frac{\sigma}{z}\right)^{10} - \frac{S}{2}\left(\frac{\sigma}{z}\right)^{4}\right] \tag{4.1}$$

with $\epsilon = 10.22$ K and $\sigma = 2.556$ Å. The surface densities n_i $(i = 1, 2)$ were taken to be the experimental values[3] $n_1 = 0.115$ Å^{-2} and $n_2 = 0.093$ Å^{-2}. The offsets z_i are such that the distance between individual solid layers and between the first solid layer and the substrate is about 3.3 Å. Our model for the solid helium layers is without doubt rather crude, in particular three important effects have been left out: zero-point motion, the core enhancement due to short-ranged correlations, and the enhanced attraction due to the presence of other particles. Both effects are clearly seen in the bulk calculation and there is no reason that they should be absent in the solid layers. In order to accommodate a possibly enhanced short-ranged attraction, we have introduced the parameter S in Eq. (4.1). The result from averaging pure Lennard-Jones potentials over a plane is obtained for $S = 1$. Instead of trying to model the three more complicated many-body effects outlined above, we have chosen to explore the possible uncertainties in the determination of the substrate potential by changing the strength parameter S within a reasonable range. The choice of the Lennard-Jones potential is slightly inconsistent with the choice of the Aziz potential[26] used for $V(|\mathbf{r}_i - \mathbf{r}_j|)$ but it has the advantage that the integrations over solid planes can be carried out analytically. Following the above discussion and in particular the comparison between the effective interaction and the Aziz potential shown in Fig. 7, we are convinced that many-body effects and zero-point motion neglected by the "fixed-substrate" approximation far outweigh any inconsistency in the particular choice of the bare interactions.

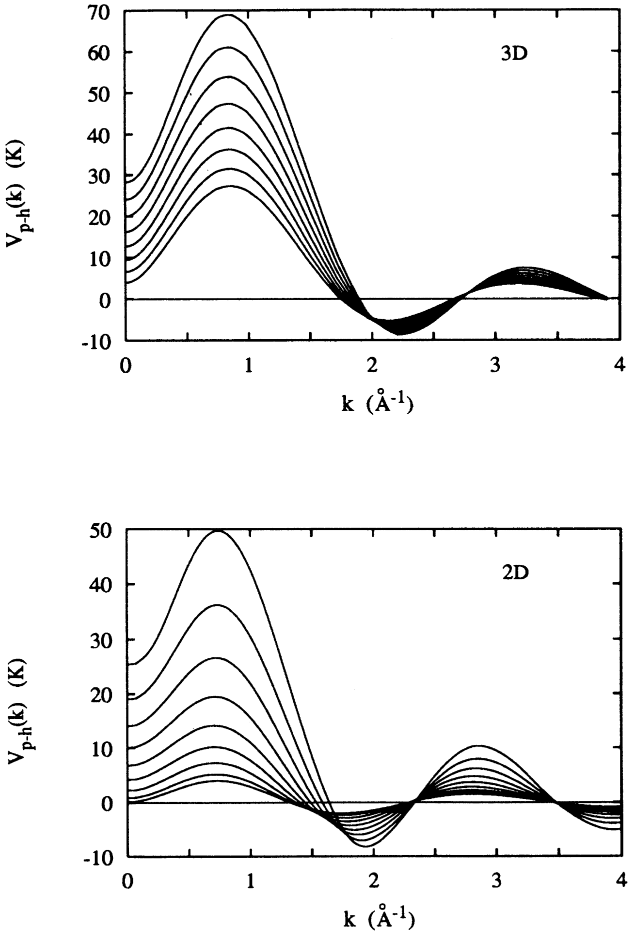

FIG. 8. The particle-hole potentials as a function of momentum for 3D and 2D *bulk* ^{4}He. The densities are the same as in Fig. 5. The function with the highest value at the origin corresponds to the highest density.

The substrate potential therefore consists of three terms,

$$U_{\rm sub}(z) = U_0(z + z_0) + \sum_{i=1}^{2} U_i(z + z_i) \tag{4.2}$$

with

$$U_0(z) = e\left[\frac{1}{15}\left(\frac{\sigma}{z}\right)^{9} - \frac{1}{2}\left(\frac{\sigma}{z}\right)^{3}\right], \tag{4.3}$$

where the strength e has been chosen to match the asymptotic strength of the graphite-helium interaction,[43] $e\sigma^3/2 = 186$ meV.

The second model considered here is a potential suggested by Dupont-Roc.[44] It describes a system where a thin film of solid H_2 of about 10 Å thickness is adsorbed to a glass surface. The ^{4}He atoms see the van der Waals force due to both the hydrogen and the glass substrate. The potential form is

$$U_{\rm sub}(z) = -\frac{435}{z^3} - \frac{1.5\times 10^4}{z^5} + \frac{0.9\times 10^6}{z^9} - \frac{915}{(z+10)^3}. \tag{4.4}$$

[$U_{\rm sub}(z)$ is given in K, and z in Å.] The last term is due to the attraction of the underlying glass surface. The shape of the substrate potentials considered here is shown in Fig. 9. We see that the "solid-helium" potential is, for $S = 1.0$, somewhat weaker than the Dupont-Roc potential, which is comparable in depth to our choice $S = 1.2$, but has a longer range. With these choices of external potentials, we cover a reasonably broad range of potential depths and strengths.

We have calculated the ground-state structure of the liquid film for surface coverages up to $n = 0.20$ Å^{-2}. As a representative set, we discuss in detail the "solid-helium" potential case, $S = 1$. As expected and described above, we *did not* find solutions for all surface coverages. In the regime of surface coverages considered here, we found *three* stable coverage regimes, corresponding to mono-, double-, and triple-layer films. Figure 10 shows representative sets of stable configurations. The first instability is encountered for coverages below $n_{\rm min} = 0.032$ Å^{-2}. Below this value, which is in the regime of uncertainties of $\rho_{2{\rm D}_{\rm min}}$ obtained from the Green's function Monte Carlo[45] and in good agreement with the variational calculations described in Sec. III, the *two-dimensional* liquid is un-

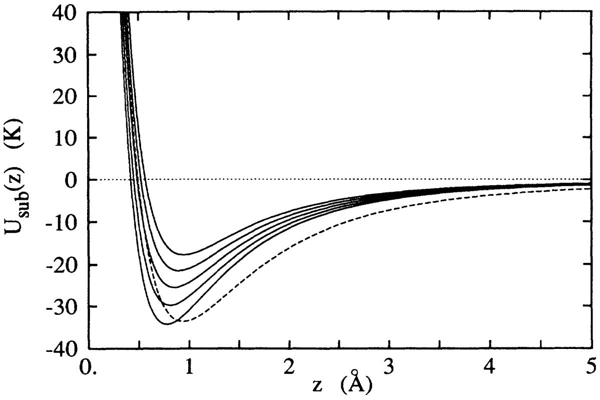

FIG. 9. The "solid helium" substrate potentials are shown for the strength parameters $S = 0.9, \ldots, S = 1.2$ (solid lines). The deepest potential corresponds to $S = 1.2$. Also shown is the Dupont-Roc potential for solid hydrogen on glass (dashed line).

stable against density fluctuations — the liquid exits in patches, above the solid layers, in coexistence with the vacuum. As the coverage is increased above $n_{\min}$, the film uniformly covers the surface; the ^{4}He film has the full planar symmetry forced on it by the substrate. Initially the film becomes more stable, but beyond a surface coverage of $0.055\ \text{Å}^{-2}$ the incompressibility drops rapidly. The cause of the rapid drop is a pronounced thickening of the monolayer which had been highly two-dimensional up to that point.

The quasi-two-dimensional phase becomes unstable at a surface coverage of about $0.068\ \text{Å}^{-2}$: for larger coverages, the film consists of a cluster-vacuum coexistence above the first liquid layer. The feature that makes ^{4}He films highly layered emerges from the realization that the instability region of the *second* layer once again has a width in coverages of $0.032\ \text{Å}^{-2}$. Beyond a coverage of $0.1\ \text{Å}^{-2}$, the second layer uniformly covers the surface. The same pattern is repeated for the third layer: an instability region with an approximate width of $0.035\ \text{Å}^{-2}$ exists between coverages of $0.13\ \text{Å}^{-2}$ and $0.165\ \text{Å}^{-2}$.

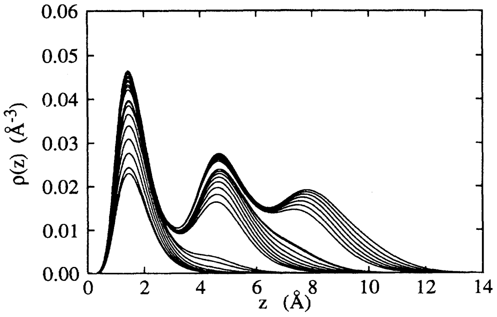

FIG. 10. The density profile for various values of coverage. The profiles correspond to stable surface coverages of 0.033, 0.035, 0.040, ..., 0.065 and 0.068 Å^{-2} for the monolayer, 0.10, 0.105, ..., 0.135 and 0.136 Å^{-2} for the double layer, and 0.165, 0.170, ..., 0.200 Å^{-2} for the triple layer.

The atomic monolayer is physically closest to the idealized situation of a two-dimensional system, we therefore devote extra attention to this case. The first quantity to look at is the correlation energy E_c as a function of coverage, and to compare this quantity with (a) a pure HNC-EL calculation within exactly the same set of approximations, and (b) exact Monte Carlo calculations for such an idealized system. The good agreement between two-dimensional HNC calculations and exact integrations of the Schrödinger equation discussed in the preceding section is important since we must verify that our approach, which has been shown to work well in three dimensions and for mixtures,[32] is also applicable in two dimensions. The comparison between the two-dimensional HNC calculation and the monolayer gives insightful information on the consequences of having an additional degree of freedom of movement perpendicular to the surface.

Figure 11 shows, for a monolayer, the comparison between our monolayer correlation energies [i.e., Eq. (2.7)] and the ground-state energies from purely two-dimensional calculations. From the comparison of the energies it appears that, for low coverages, a two-dimensional system gives a reasonable approximation for the energetics of an atomic monolayer. Expectedly, the monolayer is slightly more strongly bound. This is a natural consequence of the additional degree of freedom perpendicular to the symmetry plane allowing a closer packing of the atoms. As the coverage increases, we note, however, a characteristic *drop* in energy.

While the *general* trends and features of our comparison between a monolayer and a two-dimensional system

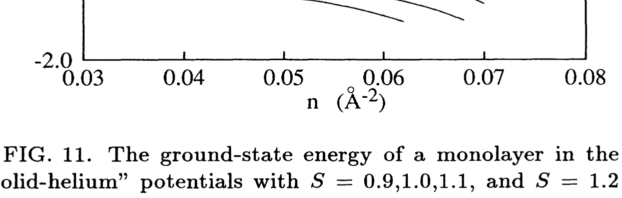

FIG. 11. The ground-state energy of a monolayer in the "solid-helium" potentials with $S = 0.9, 1.0, 1.1$, and $S = 1.2$ and on the glass-hydrogen substrate is shown as a function of surface coverage n (solid lines). The lowest line corresponds to $S = 0.9$, the highest to the glass-hydrogen substrate. Also shown is the optimized HNC-EL calculation described in Sec. II (see also Ref. 53) (long-dashed line), the Monte Carlo data of Ref. 23 (diamonds with error bars), and the two-dimensional limit of the Treiner-Pavloff (Ref. 11) energy functional (short-dashed line) for the two-dimensional limit.

are reasonable and plausible, the details of the transition described above depend apparently on both the physical nature of the system and the external field holding the particles on a plane. We have also included the prediction of an energy functional used extensively in recent work done on somewhat thicker films.[11] We see that this energy functional is far too repulsive in the limit of two dimensions. This is most likely the reason why the densities predicted by the density-functional method for the first liquid layer are significantly lower than ours.

Plots of the chemical potentials and mc_3^2 are shown in Figs. 12 and 13. Note that the incompressibilities mc_3^2 were calculated from the long-wavelength limit of the collective excitations, Eq. (2.28), and *not* as a derivative of the chemical potential, Eq. (2.31). While it is difficult to perform a reliable, numerical differentiation of the chemical potential with respect to the coverage, we see clear signatures that $d\mu/dn$ goes to zero close to the points where the collective modes become soft. The comparison between chemical potentials and sound velocities shows basically that any inconsistency of the theoretical description is insignificant. The chemical potential for the highest-coverage monolayer is notably *above* the one for the lowest-coverage double layer. This is the well-known phenomenon of *supersaturation* and *overexpansion* in a classical liquid-gas phase transition. Parenthetically, we refrained from using a Maxwell construction to map out the true equilibrium behavior (the nonmetastable portions) because of the large uncertainty involved in placing the tie lines for the high-coverage instability.

The comparison of the incompressibilities for monolayers and for a two-dimensional system shows clearly the distinction between the rigorously two-dimensional system and the atomic monolayer. Whereas the incompressibility of a two-dimensional liquid is a monotonic function of the density (cf. Fig. 2), the velocity of sound drops sharply at a coverage of about $n = 0.055\,\text{Å}^{-2}$. At this coverage the second layer becomes visibly populated (cf. Fig. 10) and the system experiences the above-mentioned drop in energy. We will see in the next section that, at the same density, the static structure functions start to differ noticeably, and in subsequent work that the physical nature of the excitations changes.

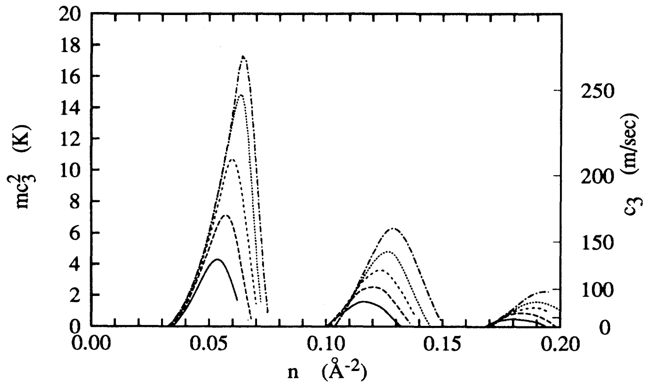

FIG. 12. The coverage dependence of the incompressibility mc_3^2 in ^{4}He films as a function of coverage and potential strength. The scale on the right side shows the corresponding sound velocity. The lines correspond to $S = 0.9$ (full), $S = 1$ (long-dashed), $S = 1.1$ (short-dashed), $S = 1.2$ (dotted line) in Eq. (4.1) and the glass-hydrogen potential (dash-dotted line).

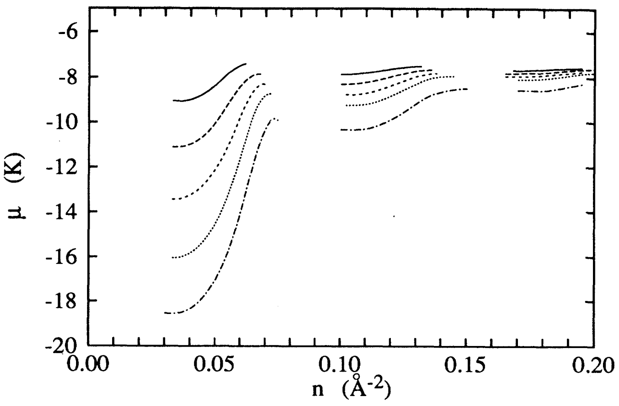

FIG. 13. Same as Fig. 12 but for the chemical potentials.

Comparison of our results with recent high-resolution adsorption isotherm data[4] indicates that Eq. (4.1) is in fact a realistic potential. The coexistence regions will obviously be strongly influenced by finite-temperature effects. Nevertheless, at 0.65 K, clearly distinguishable ^{4}He layers are observed. Vapor pressure measurements show regions of slowed rates of adsorption for coverages in regions corresponding to coexistence. The experiments also reveal well-defined oscillations in c_3, with periodicities coinciding with the formation of layers. In our calculations, inner layers continue to grow during the growth process of outer layers. For the choice $S = 1$ our first layer saturates at a density near 0.07 Å^{-2} by the time the third layer is a partial way through its growth. This value is, once again, in good agreement with the corresponding experimental value.

If the conjectured growth scenario of ^{4}He is correct, then the value of width of the instability region, $\Delta n \approx 0.035\ \text{Å}^{-2}$, should be dominated by the adsorbate-adsorbate interaction and be less influenced by the substrate-adsorbate potential. In order to verify our interpretations, we have carried out calculations varying both the *well depth* and the *range* of the substrate potential. Indeed, when the well depth is changed by varying S from 0.9 to 1.2, we find an expected overall increase in the maximum of the incompressibility, in the stable regions, indicating an increased local density per layer. We also see a slight shift of the incompressibility maximum to higher coverages. The lowest coverage for each stable region is essentially unaffected by varying S. Further, the unstable regime between the mono- and double-layer system remained of the order of $\Delta n =$ 0.030–0.035 Å^{-2}. The greatest reduction of the unstable regimes was obtained by using the somewhat longer-ranged glass-hydrogen potential.[44]

As the well-depth of the potential is increased, the "two-dimensionality" of the system is apparently en-

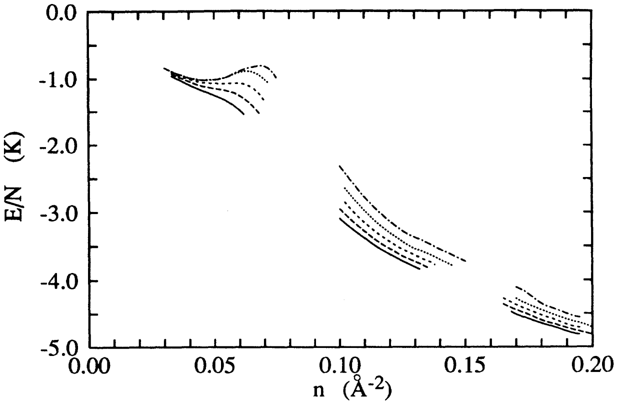

FIG. 14. Same as Fig. 12 but for the correlation energies.

hanced. This is seen in both the coverage dependence of the incompressibility — its maximum is shifted towards higher coverages — and even slightly more clearly in the correlation energy: The stronger the holding potential is, the more closely the correlation energy follows the two-dimensional curve, and the aforementioned energy drop becomes more rapid and is, in the two strongest cases, preceded by a rise in the correlation energy.

The situation is less pronounced in double- and triple-layer films. We still find incompressibility maxima and the chemical potential still exhibits supersaturation-overexpansion. The correlation energy per particle, which we show in Fig. 14 for the whole coverage range under consideration here, drops continuously and the differences between the different substrate potentials become smaller. The high-coverage limit of the correlation energy is the binding energy of the bulk liquid, which is approximately -7.2 K. Obviously we are still far from the asymptotic region.

Figure 15 shows families of stable surface coverages obtained in the glass-hydrogen potential. From the comparison with Fig. 10 it appears that the essential effect of the stronger substrate potential is that it produces more highly compressed layers, whereas the typical width of an individual layer remains essentially the same.

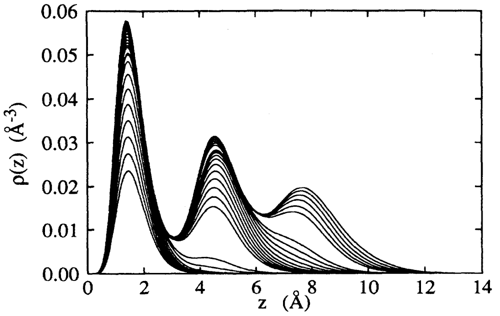

FIG. 15. The density profile for various values of coverage in the glass-hydrogen external potential. The profiles correspond to *stable* surface coverages of 0.03, 0.035, ..., 0.075 Å^{-2} for the monolayer, 0.100, 0.105, ..., 0.150 Å^{-2} for the double layer, and 0.170, 0.175, ..., 0.195 Å^{-2} for the triple layer.

V. EFFECTIVE INTERACTIONS, STRUCTURE, AND DISTRIBUTION FUNCTIONS

Further insight into the structure of the systems under consideration here and, in particular, on the differences between purely two- and three-dimensional systems and the layered structures can be gained by studying distribution and structure functions and effective interactions. While these functions in films — unlike in the bulk liquid — are not experimentally accessible quantities, they provide insight into the microscopic structure of the system and elucidate the physically important effects. All discussions in this section are based on the "solid-helium" substrate case with strength parameter $S = 1$.

We start our discussion with the pair distribution function since this has the best chance of being computed directly by Green's functions or diffusion Monte Carlo techniques. We restrict ourselves to only the *parallel* distribution function $g(z, z, r_{\|})$, i.e., to the case where both particles have the same distance from the substrate. Figure 16 shows $g(z, z, r_{\|})$ for three different monolayers and compares it with the two-dimensional calculations described in Sec. III. The difference between the rigorously two-dimensional system and the atomic monolayer is very clearly exhibited: As long as the areal density in the monolayer is low — to be specific, somewhat *below* the critical density where the incompressibility of the first layer starts to drop, the monolayer distribution functions agree reasonably well with the distribution functions predicted by the two-dimensional theory. When the areal density is increased, the monolayer distribution functions change, however, much less than those obtained from the two-dimensional calculation. It appears as if the system

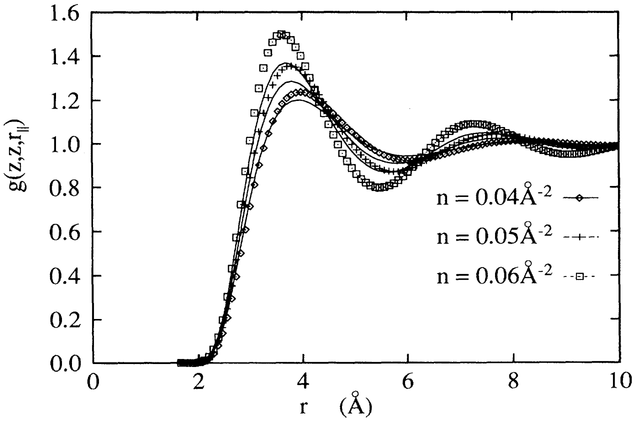

FIG. 16. The parallel pair distribution function $g(z, z, r_{\|})$ for monolayer films with coverages of $n = 0.04$ Å^{-2} (solid line), 0.05 Å^{-2}, (long-dashed line) and 0.06 Å^{-2} (short-dashed line) are compared with the corresponding calculations (diamonds, crosses, and squares) for two-dimensional ^{4}He. The monolayer distribution functions have been taken at the distance of maximum density.

starts to occupy the degree of freedom to move in the third dimension. We will see the equivalent picture when we study the static structure functions below.

The situation is not changed considerably when the second layer is added. In Fig. 17, we show the parallel distribution functions for a double-layer film. We have chosen the case $n = 0.12$ Å^{-2}, which is about the most "stable" double-layer film in the sense that mc_3^2 is largest. The distances from the substrate of $z = 2.0$ Å, 3.4 Å, and 4.8 Å correspond to the location of the *highest nearest-neighbor peak* in the first layer, the *lowest nearest-neighbor peak* between the first and second layers, and *highest nearest-neighbor peak* in the second layer. The distance 8.0 Å is far out in the asymptotic tail of the density. The first three distances correspond roughly to the distance of the first density maximum, the density minimum, and the second density maximum. Also shown are experimental values from Refs. 46 and 47, these are, on the scale of the figure, indistinguishable from our three-dimensional calculations described in Sec. III.

A number of observations can be made.

(i) The nearest-neighbor peak of the distribution function in the first layer is significantly enhanced compared with the monolayer distribution function at the same areal density; the function agrees quite well with the distribution function predicted by the two-dimensional theory for the areal density $n = 0.06$ Å^{-2}. Note that the number of particles *in the first layer* is, to the extent that this number can be defined unambiguously, not significantly increased over the monolayer situation. When compared with the *three-dimensional* distribution function, the first layer appears to be even slightly compressed.

(ii) The distribution function in the second layer resembles the one of a *three-dimensional* system of relatively low density, but agrees reasonably well with the one of a two-dimensional system with areal density between $n = 0.04$ Å^{-2} and $n = 0.05$ Å^{-2}. This supports our conclusions from our analysis of the energetics that the second layer can be thought of being, to some extent, a second two-dimensional liquid on top of the first layer.

(iii) The distribution function at the density minimum has a lower nearest-neighbor peak, but the same typical oscillations of a higher-density pair correlation function.

(iv) Only at very low densities, we find the typical shape of a low-density distribution function: A comparatively large overshoot and a long-ranged, non-oscillatory behavior.

More information on the structure of the system is revealed by studying the structure functions. We define the structure function for parallel momenta as

$$S(k_{\|}) = 1 + \frac{1}{n}\int dz dz' d^2 r_{\|} e^{i\mathbf{k}_{\|}\cdot\mathbf{r}_{\|}} \rho_1(z)\rho_1(z') \times \left[g(z,z',\mathbf{r}_{\|}) - 1\right] . \qquad (5.1)$$

This definition is suggested by the analysis of scattering experiments from inhomogeneous systems.[48,35] The (exact[50]) long-wavelength behavior of the structure function $S(k_{\|})$ defined above is $S(k_{\|}) = \hbar k/2mc_3$; our theory is consistent in the sense that we find the same relationship between the long-wavelength limit of the above structure function and the velocity of sound as defined in Eq. (2.30). The relationship is most easily proven using the normal mode representation (2.27) of the full structure function.[9,35]

Figure 18 shows a family of monolayer film structure functions and compares them with the structure functions of the two-dimensional calculations described in Sec. III. Similar to what we found for the distribution functions, we see a clear distinction between two different cases: For low coverages, ($n \approx 0.04$ Å^{-2}), the agreement between the monolayer structure function and the two-dimensional calculation is quite good. As the coverage increases to $n \approx 0.05$ Å^{-2}, the agreement becomes worse and fails completely at $n \approx 0.06$ Å^{-2}. It appears again that the discrepancies between the two-dimensional and

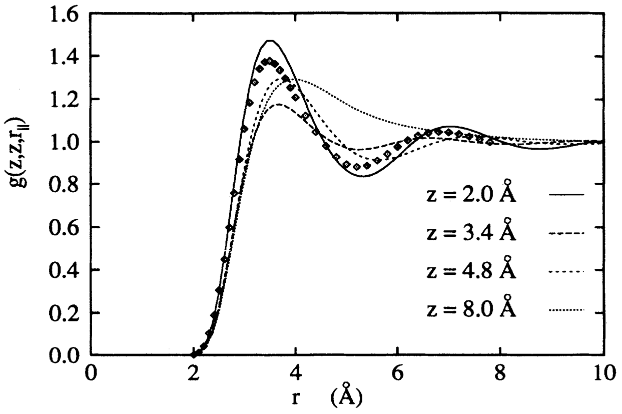

FIG. 17. The parallel pair distribution function $g(z, z, r_{\|})$ as shown for double-layer films of coverages $n = 0.12$, at distances of 2.0 Å, 3.4 Å, 4.8 Å, and 8.0 Å. Also shown in the experimental distribution function of *bulk* ^{4}He (Refs. 46 and 47) (diamonds).

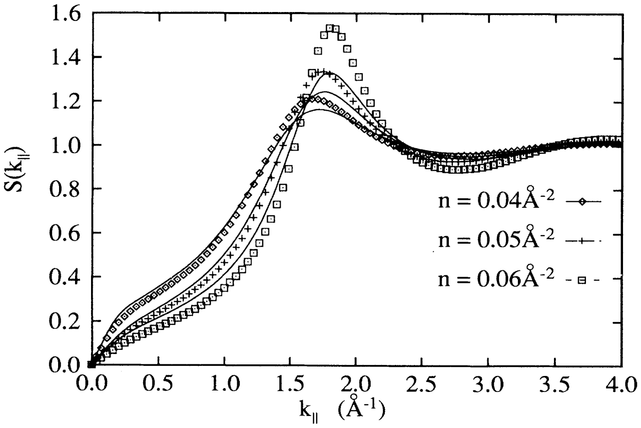

FIG. 18. The static structure functions for monolayer-films with coverages of $n = 0.04$ Å^{-2} (solid line), 0.05 Å^{-2}, (long-dashed line) and 0.06 Å^{-2} (short-dashed line) are compared with the corresponding calculations (diamonds, crosses, and squares) for two-dimensional ^{4}He.

the three-dimensional system become significant at exactly the point where the incompressibility of the system starts to *drop* as a function of coverage, i.e., where the degrees of freedom connected with the motion perpendicular to the substrate can be populated.

We finally turn to a comparison of the effective interactions between two- and three-dimensional and layered structures. A special feature of our study was that the lowest mode can become "soft" for specific coverages. Moreover, in the limit of a very thick film, the third-sound velocity should go to zero. To emphasize this feature, we show a plot of the function

$$V(k_{\|}) = \frac{1}{2}\frac{n}{\left(\sqrt{\rho_1}|[H_1(0+) + 2\tilde{V}_{\text{p-h}}(k_{\|})]^{-1}|\sqrt{\rho_1}\right)}. \quad (5.2)$$

The function has the feature that it agrees with the momentum-space particle-hole interaction in both homogeneous limits (i.e., with the functions shown in Fig. 8), and its long-wavelength limit gives the incompressibility as defined in Eq. (2.30). We start with a comparison of the monolayer results with the two-dimensional calculations, which is shown in Fig. 19. The picture we see is similar to that of the structure functions: As long as we are in the regime where the incompressibility grows as a function of the coverage, the agreement between two-dimensional and monolayer calculations is good. The turnover point is in the vicinity of coverages between $n = 0.05$ Å^{-2} and $n = 0.055$ Å^{-2}. The essential change we see as the coverage is further increased is a rapid drop in the long-wavelength portion of the effective interaction indicating the approaching instability. This, in turn, is related to the first appearance of a true surface excitation.

Figure 20 finally shows $V(k_{\|})$ for double- and triple-layer films of coverages $n = 0.12$ Å^{-2}, $n = 0.17$ Å^{-2}, and $n = 0.180$ Å^{-2} and provides a comparison with the bulk three-dimensional calculation at density $\rho = 0.022$ Å^{-3}.

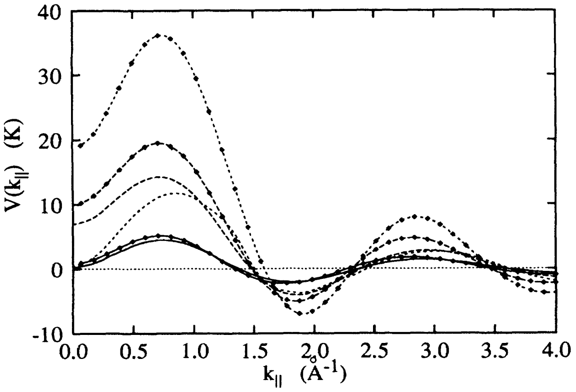

FIG. 19. The effective interaction, as defined in Eq. (5.2), is shown for monolayer films with coverages of $n = 0.035$ Å^{-2} (solid line), 0.055 Å^{-2} (long-dashed line), and 0.067 Å^{-2} (short-dashed line). Also shown are the results from two-dimensional calculations for the same coverages (marked lines).

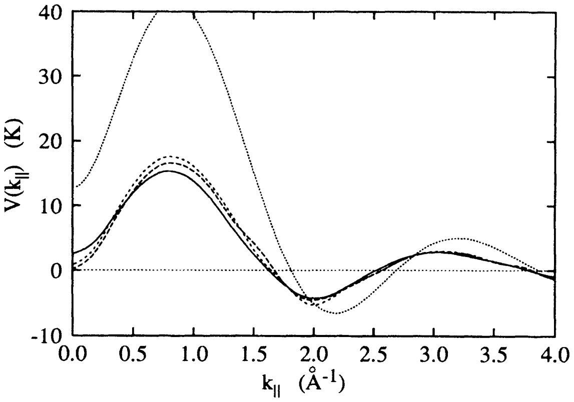

FIG. 20. The effective interaction, as defined in Eq. (5.2), is shown for multilayer films with coverages of $n = 0.120$ Å^{-2} (solid line), 0.170 Å^{-2} (long-dashed line), and 0.180 Å^{-2} (short-dashed line). Also shown is the particle-hole interaction the results from a three-dimensional bulk calculation at a density of $\rho = 0.022$ Å^{-3} (dotted line).

The coverages used here have been chosen to represent a "very stable" double-layer film ($n = 0.12$ Å^{-2}), a triple-layer film close to its instability at the low-end coverage ($n = 0.17$ Å^{-2}) and a stable triple-layer film ($n = 0.18$ Å^{-2}). The most significant observation is that all of these interactions are still far from the bulk limit. This may to some extent be due to our choice of representation — definition (5.2) emphasizes the long-wave limit of the interaction, which is zero in the thick-film limit. But the discrepancy is also an indication that we are dealing still with a rather low-density system. Note that the three-dimensional particle-hole interaction depends sensitively on the density, cf. Fig. 8.

Otherwise, the three different surface cases are almost identical. The part responsible for the stability of the film is the long-wavelength limit, which is identical to the incompressibilities shown in Fig. 12. It is evident that this long-wavelength limit is a result of significant cancellations between the repulsive and the attractive parts of the effective interaction. The cancellations become increasingly more complete as the thickness of the film increases. While we are confident that our results are significant, any small diagrammatic inconsistency in the theory and any small numerical inaccuracy will be enhanced and calculations of the specific quantity (2.30) in the high-coverage limit will become increasingly difficult.

VI. SUMMARY AND OUTLOOK

We have discussed in this paper the energetics of adsorbed films of ^{4}He and have studied in particular the question of "how two dimensional" an atomic monolayer is. Our results on monolayers are perhaps the most revealing since they show a sharp transition at a point where the degree of freedom of moving in the third direction becomes relevant. The transition is indicated by a rather sudden drop in the incompressibility. The situation is repeated more weakly in a second layer, and also in a third one. The general features of the systems studied here are reasonably stable against changes of both the width and the range of the substrate potential. It appears that the systems are, in a longer-range potential, somewhat more stable in the sense that the regime of unstable coverages is reduced.

We have concentrated on an exploration of the phenomena, restricting the theoretical discussion to a bare minimum. The new *theoretical* aspect of our work is the inclusion of triplet correlations, which is necessary to make the predictions of our theory quantitative. These correlations have the effect of making the equation of state somewhat stiffer compared with earlier calculations done within the pure HNC approximation,[49,9] and are partly responsible for generating the phase transitions discussed in this work. There are still a number of interesting formal questions to be solved, in particular in connection with the calculation of the (third) sound velocity. But the basic structure of the theory will and should remain unchanged. A particularly strong indication for the adequacy of our approach is that any physical instability of the system appears intrinsically and *a priori* by the fact that the HNC-EL energy functional ceases to exist, and not *a posteriori* in the sense that one might find a negative $d\mu/dn$ and then conclude that the system is unstable, even if there are no indications for such an instability in the calculational scheme.

In terms of the energetics, there appears to be little room for improvement: Both limits (i.e. the homogeneous two- and three-dimensional systems) which we have been able to compare agree well with Monte Carlo data over the full range of densities considered here. This exhausts the only available means to uncover any sources of *theoretical* uncertainties. For the complicated geometry numerical sacrifices are necessary: For the solution of the inhomogeneous Euler equations all functions were discretized on a mesh of typically 0.2 Å (in coordinate space) and 0.2 Å^{-1} in momentum space, with cutoffs of the pair functions at approximately 15 Å and 15 Å^{-1}. In contrast, our bulk calculations were carried out on a mesh about twice as fine, and twice as large. The computational effort for such discretizations remains rather modest and can, in principle, be carried out on personal computer. The most time-consuming part is the calculation of triplet correlations. In summary, we do not expect that better calculations of the ground-state structure will reveal a significantly different physical picture.

Our results for the sound velocity compare directly to the measurements of Zimmerli *et al.* (Ref. 4). These authors report, starting with the fourth layer, an oscillating behavior of the third-sound velocity. The fourth layer of these experiments should be compared with our second *liquid* layer since we have modeled the first two *solid* layers by a static potential. The maximum sound velocity is found to be of the order of 35 m/sec, dropping, in the next layer, somewhat below 30 m/sec. These values are somewhat smaller than ours as shown in Fig. 12. However, Fig. 12 also shows that, at these coverages, the sound velocity is a sensitive function of the substrate potential, a change of the potential strength by 20% (from $S = 0.9$ to $S = 1.1$) can change the sound velocity by a factor of 2. We *do not* believe that the simple model for the solid layers chosen here, or any other substrate potential developed along the same line of arguments, can presently claim an accuracy of better than 10%. Figures 7 and 8 provide a vivid demonstration of the importance of many-body contributions to effective interactions and their density dependence. Rather, it appears at this point to be more appropriate to use experimental sound velocities as a measure for the strength of the substrate potential.

A number of interesting physical effects are apparent from our discussion of the energetics and growth mechanisms. Whenever a physical system approaches a phase transition, this comes with the "softening" of an excitation. In the present situation, the "soft modes" would correspond to physically different types of excitations: At the low-coverage end of each stable region, the soft modes should correspond to excitations *within* the symmetry plane, whereas at the high-coverage end, the soft excitations would correspond to particles moving *out of* the symmetry plane. These different mechanisms should be reflected in the local particle motion in each of these excitations. Finally, the different types of excitation mechanisms should be reflected in the thermodynamic properties of thin films.

The physical nature of excitations can be studied and discussed qualitatively at the level of the Feynman theory[50] of collective excitations.[48,35] However, an interesting consequence of the physical scenario requires a more advanced theory: Along with instability comes an area in which the corresponding soft mode has anomalous dispersion. This means that a phonon-ripplon of higher energy can, in principle, decay into two or more excitations of lower energy and longer wavelength. A treatment of this effect requires the inclusion of multiphonon processes. Such processes, which can be described within the theory of correlated basis functions[29] or time-dependent correlation functions,[51] will be discussed in a forthcoming paper.

ACKNOWLEDGMENTS

The work was supported, in part, by the North Atlantic Treaty Organization (to B.E.C), the National Science Foundation under Grant Nos. PHY-9108066 and INT-9014040 (to E.K.), and the Academy of Finland (to M.S). E.K. thanks the Institute Laue-Langevin for hospitality where this work was started. Some computational resources were provided by the Minnesota Supercomputer Institute. Discussions with G. Agnolet, E. Bashkin, C. E. Campbell, H.-J. Lauter, and W. M. Saslow are gratefully acknowledged.

APPENDIX: TRIPLET CORRELATIONS

In this appendix, we give a brief account of the derivation of the triplet energy and the triplet Euler equation for a nonuniform system. Since this is the first time that the triplet equations are formulated for a nonuniform system, we have to start from the wave function (2.2). Using the Jackson-Feenberg identity

$$\int d^3r_1 \cdots d^3r_N \Psi_0 \nabla_i^2 \Psi_0 \equiv \frac{1}{2} \int d^3r_1 \cdots d^3r_N \Psi_0^2 \nabla_i^2 \ln \Psi_0, \tag{A1}$$

we can write the total variational energy as

$$E_0 = \Delta E_1^* + \Delta E_2^* + \Delta E_3^*, \tag{A2}$$

where

$$\Delta E_1^* = \int d^3r \rho_1(\mathbf{r}) \left[U_{\rm ext}(\mathbf{r}) - \frac{\hbar^2}{8m} \nabla^2 u_1(\mathbf{r}) \right], \tag{A3}$$

$$\Delta E_2^* = \frac{1}{2!} \int d^3r_1 d^3r_2 \rho_2(\mathbf{r}_1, \mathbf{r}_2) \left[v(|\mathbf{r}_1 - \mathbf{r}_2|) - \frac{\hbar^2}{8m} (\nabla_1^2 + \nabla_2^2) u_2(\mathbf{r}_1, \mathbf{r}_2) \right], \tag{A4}$$

and

$$\Delta E_3^* = -\frac{1}{3!} \frac{\hbar^2}{8m} \int d^3r_1 d^3r_2 d^3r_3 \rho_3(\mathbf{r}_1, \mathbf{r}_2, \mathbf{r}_3) \left[\nabla_1^2 + \nabla_2^2 + \nabla_3^2 \right] u_3(\mathbf{r}_1, \mathbf{r}_2, \mathbf{r}_3). \tag{A5}$$

Here, we have introduced the n-particle ($n = 1, 2, 3$) densities

$$\rho_n(\mathbf{r}_1, \ldots, \mathbf{r}_n) = \frac{N!}{(N-n)!} \frac{\int d^3r_{n+1} \cdots d^3r_N \Psi_0^2(\mathbf{r}_1, \ldots, \mathbf{r}_N)}{\int d^3r_1 \cdots d^3r_N \Psi_0^2(\mathbf{r}_1, \ldots, \mathbf{r}_N)}. \tag{A6}$$

Other useful quantities are the n-body distribution functions

$$g_n(\mathbf{r}_1, \ldots, \mathbf{r}_n) = \frac{\rho_n(\mathbf{r}_1, \ldots, \mathbf{r}_n)}{\rho_1(\mathbf{r}_1) \cdots \rho_1(\mathbf{r}_n)}. \tag{A7}$$

We next use the Born-Green-Yvon equation to eliminate the one-body function $u_1(\mathbf{r})$:

$$\nabla_1 \rho_1(\mathbf{r}_1) = \rho_1(\mathbf{r}_1) \nabla_1 u_1(\mathbf{r}_1) + \int d^3r_2 \rho_2(\mathbf{r}_1, \mathbf{r}_2) \nabla_1 u_2(\mathbf{r}_1, \mathbf{r}_2) + \frac{1}{2} \int d^3r_2 d^3r_3 \rho_3(\mathbf{r}_1, \mathbf{r}_2\mathbf{r}_3) \nabla_1 u_3(\mathbf{r}_1, \mathbf{r}_2, \mathbf{r}_3). \tag{A8}$$

With this, we can rewrite the total ground-state energy as

$$E_0 = \Delta E_1 + \Delta E_2 + \Delta E_3 \tag{A9}$$

with

$$\Delta E_1 = \int d^3r \left\{ \rho_1(\mathbf{r}) U_{\rm sub}(\mathbf{r}) + \frac{\hbar^2}{2m} \left| \nabla \sqrt{\rho_1(\mathbf{r})} \right|^2 \right\}, \tag{A10}$$

$$\Delta E_2 = \frac{1}{2!} \int d^3r_1 d^3r_2 \rho_2(\mathbf{r}_1, \mathbf{r}_2) \left\{ v(|\mathbf{r}_1 - \mathbf{r}_2|) - \frac{\hbar^2}{8m} \left[D(\mathbf{r}_1) + D(\mathbf{r}_2) \right] u_2(\mathbf{r}_1, \mathbf{r}_2) \right\}, \tag{A11}$$

and

$$\Delta E_3 = -\frac{1}{3!} \frac{\hbar^2}{8m} \int d^3r_1 d^3r_2 d^3r_3 \rho_3(\mathbf{r}_1, \mathbf{r}_2, \mathbf{r}_3) \left[D(1) + D(2) + D(3) \right] u_3(\mathbf{r}_1, \mathbf{r}_2, \mathbf{r}_3), \tag{A12}$$

where

$$D(\mathbf{r}_i) = \frac{1}{\rho_1(\mathbf{r}_i)} \nabla_i \cdot \rho_1(\mathbf{r}_i) \nabla_i. \tag{A13}$$

The relation between the two-body density and the two-body correlation factor is provided by the inhomogeneous hypernetted-chain equations:

$$g_2(\mathbf{r}_1, \mathbf{r}_2) = \exp\left[u_2(\mathbf{r}_1, \mathbf{r}_2) + N(\mathbf{r}_1, \mathbf{r}_2) + E(\mathbf{r}_1, \mathbf{r}_2) \right], \tag{A14}$$

$$
\begin{aligned}
&h(\mathbf{r}_1,\mathbf{r}_2) \equiv g(\mathbf{r}_1,\mathbf{r}_2) - 1,\\
&X(\mathbf{r}_1,\mathbf{r}_2) \equiv h(\mathbf{r}_1,\mathbf{r}_2) - N(\mathbf{r}_1,\mathbf{r}_2), \qquad \text{(A15)}\\
&N(\mathbf{r}_1,\mathbf{r}_2) = [h * X]\,(\mathbf{r}_1,\mathbf{r}_2).
\end{aligned}
$$

Expressions (A14) and (A15) are exact. The level of sophistication of the theory is defined by the choice of the approximation for the "elementary diagram sum" $E(\mathbf{r}_1,\mathbf{r}_2)$, which is represented as an infinite series of diagrams in terms of the pair distribution function $h(\mathbf{r}_i,\mathbf{r}_j)$. The set of elementary diagrams included in the calculation determines both the computational effort and the precision of the predictions of the theory. The HNC equations do not change in the presence of triplet correlations, only the definition of the "elementary diagrams" needs to be generalized. The simplest choice is the "HNC approximation," $E(\mathbf{r}_1,\mathbf{r}_2) = 0$ and no triplet correlations. This is also the simplest approximation that allows for a meaningful optimization of the ground-state correlations.

Since the pair correlation function $u_2(\mathbf{r}_1,\mathbf{r}_2)$ appears explicitly only in Eq. (A14) and all elementary diagrams can be expressed in terms of the two-body distribution function $g_2(\mathbf{r}_1,\mathbf{r}_2)$, it is advantageous to use Eq. (A14) to eliminate the pair correlations $u_2(\mathbf{r}_1,\mathbf{r}_2)$ from the energy expression (A11):

$$
\begin{aligned}
(\Delta E_2) &= E_R + E_Q + E_E\\
&= \frac{1}{2}\int d^3r_1 d^3r_2 \rho_1(\mathbf{r}_1)\rho_1(\mathbf{r}_2)\left[g(\mathbf{r}_1,\mathbf{r}_2)v(|\mathbf{r}_1-\mathbf{r}_2|) + \frac{\hbar^2}{2m}\left[\left|\boldsymbol{\nabla}_1\sqrt{g_2(\mathbf{r}_1,\mathbf{r}_2)}\right|^2 + \left|\boldsymbol{\nabla}_2\sqrt{g_2(\mathbf{r}_1,\mathbf{r}_2)}\right|^2\right]\right]\\
&\quad + \frac{\hbar^2}{16m}\int d^3r_1 d^3r_2 \rho_1(\mathbf{r}_1)\rho_1(\mathbf{r}_2) h(\mathbf{r}_1,\mathbf{r}_2)\left[D(\mathbf{r}_1)+D(\mathbf{r}_2)\right] N(\mathbf{r}_1,\mathbf{r}_2)\\
&\quad + \frac{\hbar^2}{16m}\int d^3r_1 d^3r_2 \rho_1(\mathbf{r}_1)\rho_1(\mathbf{r}_2) h(\mathbf{r}_1,\mathbf{r}_2)\left[D(\mathbf{r}_1)+D(\mathbf{r}_2)\right] E(\mathbf{r}_1,\mathbf{r}_2), \qquad \text{(A16)}
\end{aligned}
$$

where E_E and E_Q are the last and next-to-the-last terms, respectively. It is now straightforward to derive the Euler equation for the density and the pair correlations. The relevant manipulations have been described in various places (cf. Refs. 8 and 49), we focus here on the treatment of the triplet correlations. Two procedures can be used to derive Euler equations for the triplet correlations: One is to start from the energy expressions (A11) and (A12), choose the set of elementary diagrams and the approximation for the three-body distribution function which one is prepared to calculate, and derive a Euler equation for the triplet correlation function from this approximate energy functional. The alternative is to start with the most general Euler equation and derive the exact expression for the optimal triplet function. Given the exact Euler equation one can identify the approximations and a corresponding energy functional that preserve the structure of this equation. These manipulations have been carried out, for the uniform case and for mixtures, at great length in Refs. 28–30 and 32. The case of the nonuniform system is technically somewhat more complicated due to the loss of translational invariance. But the topological structure of the diagrams necessary to obtain an energy functional which is consistent with the exact energy functional is the same. We proceed therefore with the somewhat easier route and start with an approximate energy functional.

Triplet correlations appear in the energy functional in three places: Explicitly in the three-body kinetic energy (A12) and implicitly in the elementary diagrams and three-body distribution function. We can split the elementary diagrams into two types:

$$E(\mathbf{r}_1,\mathbf{r}_2) = E^{(2)}(\mathbf{r}_1,\mathbf{r}_2) + E^{(3)}(\mathbf{r}_1,\mathbf{r}_2) \qquad \text{(A17)}$$

where $E^{(2)}(\mathbf{r}_1,\mathbf{r}_2)$ is the set of elementary diagrams that can be expressed in terms of the pair-distribution function $g_2(\mathbf{r}_1,\mathbf{r}_2)$ alone, and $E^{(3)}(\mathbf{r}_1,\mathbf{r}_2)$ contains diagrams in which explicit three-body correlations appear. Using the same division we then write the energy contribution E_E as

$$E_E = E_E^{(2)} + E_E^{(3)} \qquad \text{(A18)}$$

with

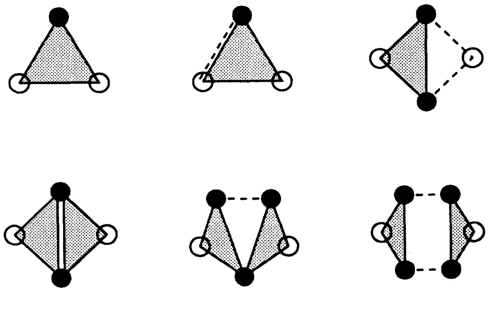

FIG. 21. The diagrammatic representation of the elementary diagrams containing triplet correlations which are included in our triplet energy expression (A27). The dashed line represents a pair distribution function $h(\mathbf{r}_i,\mathbf{r}_j) = g(\mathbf{r}_i,\mathbf{r}_j) - 1$, and the shaded triangle represents the triplet correlation function $u_3(\mathbf{r}_1,\mathbf{r}_2,\mathbf{r}_3)$, and the solid dots coordinate space integrations $\int d^3r_i\rho_1(\mathbf{r}_i)$.

$$E_E^{(i)} = \frac{\hbar^2}{16m}\int d^3r_1 d^3r_2 \rho_1(\mathbf{r}_1)\rho_1(\mathbf{r}_2)h(\mathbf{r}_1,\mathbf{r}_2)\left[D(\mathbf{r}_1)+D(\mathbf{r}_2)\right]E_E^{(i)}(\mathbf{r}_1,\mathbf{r}_2) \tag{A19}$$

for $i = 2, 3$. The triplet energy is then the sum of the explicit contribution of the triplet correlations and the piece coming from the elementary diagrams:

$$\Delta E^{(3)} = E_E^{(3)} + \Delta E_3, \tag{A20}$$

where ΔE_3 is given in Eq. (A12).

It is now time to specify the set of diagrams which we include in $E^{(3)}(\mathbf{r}_1,\mathbf{r}_2)$ and the three-body distribution function $g_3(\mathbf{r}_1,\mathbf{r}_2,\mathbf{r}_3)$. These diagrams are shown in Figs. 21 and 22. We also expand $\exp\left[u_3(\mathbf{r}_1,\mathbf{r}_2,\mathbf{r}_3)\right] \approx 1 + u_3(\mathbf{r}_1,\mathbf{r}_2,\mathbf{r}_3)$. Combining the energy expressions from elementary diagrams and triplet correlations leads, after a somewhat tedious algebra,[21,22] to the expression

$$\begin{aligned}\Delta E^{(3)} = {} & \frac{1}{12}\int d^3r_1 d^3r_2 d^3r_3 \tilde{u}_3(\mathbf{r}_1,\mathbf{r}_2,\mathbf{r}_3)\tilde{W}_3(\mathbf{r}_1,\mathbf{r}_2,\mathbf{r}_3) \\ & +\frac{1}{24}\int d^3r_1\cdots d^3r_6 \tilde{u}_3(\mathbf{r}_1,\mathbf{r}_2,\mathbf{r}_3)\Big\{H_1(1)\delta(\mathbf{r}_1-\mathbf{r}_4)S(\mathbf{r}_2,\mathbf{r}_5)S(\mathbf{r}_3,\mathbf{r}_6) + \text{cycl.}\Big\}\tilde{u}_3(\mathbf{r}_4,\mathbf{r}_5,\mathbf{r}_6)\end{aligned} \tag{A21}$$

with

$$\begin{aligned}\tilde{W}_3(\mathbf{r}_1,\mathbf{r}_2,\mathbf{r}_3) = {} & -\frac{\hbar^2}{2m}\sqrt{\rho_1(\mathbf{r}_1)\rho_1(\mathbf{r}_2)\rho_1(\mathbf{r}_3)}\Bigg\{\left[\boldsymbol{\nabla}_1 h(\mathbf{r}_1,\mathbf{r}_2)\cdot\boldsymbol{\nabla}_1 h(\mathbf{r}_1,\mathbf{r}_3) + \text{cycl.}\right] \\ & + \int d^3r_4 \rho_1(\mathbf{r}_4)\left[h(\mathbf{r}_4,\mathbf{r}_1)\boldsymbol{\nabla}_4 h(\mathbf{r}_4,\mathbf{r}_2)\cdot\boldsymbol{\nabla}_4 h(\mathbf{r}_4,\mathbf{r}_3) + \text{cycl.}\right]\Bigg\}\end{aligned} \tag{A22}$$

and the usual tilde notation

$$\tilde{u}_3(\mathbf{r}_1,\mathbf{r}_2,\mathbf{r}_3) = \sqrt{\rho_1(\mathbf{r}_1)\rho_1(\mathbf{r}_2)\rho_1(\mathbf{r}_3)}u_3(\mathbf{r}_1,\mathbf{r}_2,\mathbf{r}_3). \tag{A23}$$

The triplet energy is quadratic in $\tilde{u}_3(\mathbf{r}_1,\mathbf{r}_2,\mathbf{r}_3)$, it is easily minimized with respect to the triplet function. The resulting (linear) Euler equation for $\tilde{u}_3(\mathbf{r}_1,\mathbf{r}_2,\mathbf{r}_3)$ can be most conveniently solved in the basis of Feynman phonon states $\psi^{(l)}$ and $\phi^{(l)}$ defined by the eigenvalue problems (2.23) and (2.25). Let

$$\tilde{V}_{mno} = \int d^3r_1 d^3r_2 d^3r_3 \tilde{W}_3(\mathbf{r}_1,\mathbf{r}_2,\mathbf{r}_3)\psi^{(m)}(\mathbf{r}_1)\psi^{(n)}(\mathbf{r}_2)\psi^{(o)}(\mathbf{r}_3) \tag{A24}$$

and

$$\tilde{u}_{mno} = \int d^3r_1 d^3r_2 d^3r_3 \tilde{u}_3(\mathbf{r}_1,\mathbf{r}_2,\mathbf{r}_3)\phi^{(m)}(\mathbf{r}_1)\phi^{(n)}(\mathbf{r}_2)\phi^{(o)}(\mathbf{r}_3). \tag{A25}$$

In this basis, the triplet correlation function is given by

$$\tilde{u}_{mno} = \frac{\tilde{V}_{mno}}{\hbar(\omega_m+\omega_n+\omega_o)} \tag{A26}$$

and, reinserting the solution into Eq. (A21), we find the triplet energy

$$\Delta E^{(3)} = -\frac{1}{24}\sum_{mno}\frac{\left|\tilde{V}_{mno}\right|^2}{\hbar(\omega_m+\omega_n+\omega_o)}. \tag{A27}$$

The remaining task is to work out the matrix elements $\tilde{V}_{mno}$. For this purpose, recall Eq. (2.27) and the consequence

$$\tilde{h}(\mathbf{r},\mathbf{r}') = \sum_m \phi^{(m)}(\mathbf{r})\phi^{(m)}(\mathbf{r}') - \delta(\mathbf{r}-\mathbf{r}') = \sum_m\left[\phi^{(m)}(\mathbf{r}) - \psi^{(m)}(\mathbf{r})\right]\phi^{(m)}(\mathbf{r}'), \tag{A28}$$

and therefore,

$$\tilde{V}_{mno} = -\frac{\hbar^2}{2m}\int d^3r\Big\{\xi^{(m)}(\mathbf{r})\boldsymbol{\nabla}\zeta^{(n)}(\mathbf{r})\cdot\boldsymbol{\nabla}\zeta^{(o)}(\mathbf{r}) + \text{cycl.}\Big\}, \tag{A29}$$

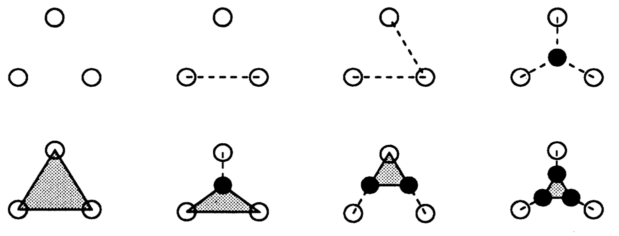

FIG. 22. The diagrammatic representation of the three-body distribution function $g(\mathbf{r}_1, \mathbf{r}_2, \mathbf{r}_3)$ in terms of pair distribution functions $h(\mathbf{r}_i, \mathbf{r}_j) = g(\mathbf{r}_i, \mathbf{r}_j) - 1$ (solid lines) and an irreducible triplet function $X_3(\mathbf{r}_1, \mathbf{r}_2, \mathbf{r}_3)$ (shaded triangle).

where we have abbreviated

$$\xi^{(m)}(\mathbf{r}) \equiv \sqrt{\rho_1(\mathbf{r})}\phi^{(m)}(\mathbf{r}), \tag{A30}$$

$$\zeta^{(m)}(\mathbf{r}) \equiv \frac{\phi^{(m)}(\mathbf{r}) - \psi^{(m)}(\mathbf{r})}{\sqrt{\rho_1(\mathbf{r}_1)}}. \tag{A31}$$

With these manipulations, we have generalized the theory of optimized three-particle correlations[28–30] to nonuniform systems. What is as important as the derivation of the generalized formulas is the fact that these quantities can be calculated with a reasonable numerical effort. To find the corrections to the potentials it is convenient to start with the energy (A21) and (A22). Since we have optimized the triplet functions, we do not need to vary them with respect to their density dependence. The calculations are analytically tedious, but straightforward and shall not be reproduced here.

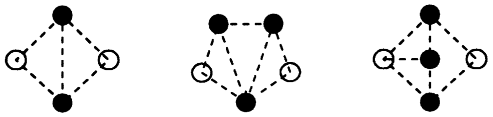

FIG. 23. The diagrammatic representation of the first few contributions to the sum of all elementary diagrams. The four-body diagram has been used for the calculation of the scaling factor, whereas both the four-body and the two first five-body diagrams are included in the bulk approximation.

---

[1] H. J. Lauter *et al.*, Surf. Sci. **125**, 265 (1983).

[2] H. J. Lauter, H. Godfrin, and H. Wiechert, in *Proceedings of the Second International Conference on Phonon Physics*, edited by J. Kollàr, N. Kroo, M. Meynhard, and T. Siklos (World Scientific, Singapore, 1985), p. 842.

[3] H. J. Lauter, H. Godfrin, V. L. P. Frank, and P. Leiderer, in *Excitations in Two-Dimensional and Three-Dimensional Quantum Fluids*, Vol. 257 of NATO Advanced Study Institute, Series B: Physics, edited by A. F. G. Wyatt and H. J. Lauter (Plenum, New York, 1991), p. 419.

[4] G. Zimmerli, G. Mistura, and M. H. W. Chan, Phys. Rev. Lett. **68**, 60 (1992).

[5] P. J. Shirron and J. M. Mochel, Phys. Rev. Lett. **67**, 1118 (1991).

[6] K. S. Ketola, S. Wang, and R. B. Hallock, Phys. Rev. Lett. **68**, 201 (1992).

[7] P. J. Nacher and J. Dupont-Roc, Phys. Rev. Lett. **67**, 2966 (1991).

[8] E. Krotscheck, Q.-X. Qian, and W. Kohn, Phys. Rev. B **31**, 4245 (1985).

[9] J. L. Epstein and E. Krotscheck, Phys. Rev. B **37**, 1666 (1988).

[10] M. Wagner and D. Ceperley, Bull. Am. Phys. Soc **36**, 825 (1991).

[11] N. Pavloff and J. Treiner, J. Low Temp. Phys. **83**, 331 (1991).

[12] E. Cheng, M. W. Cole, W. F. Saam, and J. Treiner, Phys. Rev. B **46**, 13967 (1992).

[13] J. Dupont-Roc, M. Himbert, N. Pavloff, and J. Treiner, J. Low Temp. Phys. **83**, 31 (1990).

[14] G. Ihm, M. W. Cole, F. Toigo, and J. R. Klein, Phys. Rev. A **42**, 5244 (1990).

[15] E. Cheng, G. Ihm, and M. W. Cole, J. Low Temp. Phys. **74**, 519 (1989).

[16] E. Cheng, M. Cole, W. Saam, and J. Treiner, Phys. Rev. Lett. **67**, 1007 (1991).

[17] E. Cheng *et al.*, Physica A **177**, 466 (1991).

[18] E. Cheng, M. W. Cole, and P. Shaw, J. Low Temp. Phys. **82**, 49 (1991).

[19] J. F. Annett, M. W. Cole, P. Shaw, and R. Stratt, J. Low Temp. Phys. **84**, 1 (1991).

[20] B. E. Clements, E. Krotscheck, and H. J. Lauter, Phys. Rev. Lett. **70**, 1287 (1993).

[21] J. L. Epstein, Ph.D. thesis, Texas A& M University, 1992 (unpublished).

[22] B. E. Clements, J. L. Epstein, E. Krotscheck, and C. J. Tymczak (unpublished).

[23] P. A. Whitlock, G. V. Chester, and M. H. Kalos, Phys. Rev. B **38**, 2418 (1988).

[24] R. de Bruyn Ouboter and C. N. Yang, Physica B **144**, 127 (1986).

[25] M. J. McKenna, T. B. Brosius, and J. D. Maynard, Phys. Rev. Lett. **69**, 3346 (1992).

[26] R. A. Aziz *et al.*, J. Chem. Phys. **70**, 4330 (1979).

[27] E. Feenberg, *Theory of Quantum Liquids* (Academic, New York, 1969).

[28] C. E. Campbell, Phys. Lett. **44A**, 471 (1973).

[29] C. C. Chang and C. E. Campbell, Phys. Rev. B **15**, 4238 (1977).

[30] E. Krotscheck, Phys. Rev. B **33**, 3158 (1986).

[31] C. E. Campbell and E. Feenberg, Phys. Rev. **188**, 396 (1969).

[32] E. Krotscheck and M. Saarela, Phys. Rep. **232**, 1 (1993).

[33] E. Krotscheck, Phys. Rev. B **31**, 4258 (1985).

[34] A. D. Jackson, A. Lande, and L. Lantto, Nucl. Phys. A **317**, 1 (1979).

[35] E. Krotscheck and C. J. Tymczak, Phys. Rev. B **45**, 217 (1992).

[36] K. R. Atkins, Physica **23**, 1143 (1957).

[37] K. R. Atkins, Phys. Rev. **113**, 962 (1959).

[38] D. Goodstein, Phys. Rev. **183**, 327 (1969).

[39] A. D. Jackson, B. K. Jennings, A. Lande, and R. A. Smith, Phys. Rev. B **24**, 105 (1981).

[40] M. Saarela and J. Suominen, in *Condensed Matter Theories*, edited by J. S. Arponen, R. F. Bishop, and M. Manninen (Plenum, New York, 1988), Vol. 3, p. 157.

[41] P. Roach, J. Ketterson, and C. Woo, Phys. Rev. A **2**, 543 (1970).

[42] C. H. Aldrich and D. Pines, J. Low Temp. Phys. **25**, 677 (1976).

[43] M. W. Cole, D. R. Frankl, and D. L. Goodstein, Rev. Mod. Phys. **53**, 199 (1981).

[44] J. Dupont-Roc (private communication).

[45] The value 0.037 $Å^{-2}$ follows from computing the compressibility from the equation of state in Ref. 23.

[46] E. C. Svensson, V. F. Sears, A. D. B. Woods, and P. Martel, Phys. Rev. B **21**, 3638 (1980).

[47] H. N. Robkoff and R. B. Hallock, Phys. Rev. B **24**, 159 (1981).

[48] S. A. Chin and E. Krotscheck, Phys. Rev. B **45**, 852 (1992).

[49] E. Krotscheck, Phys. Rev. B **32**, 5713 (1985).

[50] R. P. Feynman, Phys. Rev. **94**, 262 (1954).

[51] M. Saarela, Phys. Rev. B **33**, 4596 (1986).

[52] C. Ebner and D. O. Edwards, Phys. Rep. **2**, 77 (1971).

[53] M. Saarela, in *Recent Progress in Many Body Theories*, edited by Y. Avishai (Plenum, New York, 1990), Vol. 2, p. 337.